

1 **The interactive global fire module pyrE (v1.0)**

2 Keren Mezuman^{1,2}, Kostas Tsigaridis^{1,2}, Gregory Faluvegi^{1,2}, Susanne E. Bauer^{2,1}

3 ¹ Center for Climate Systems Research, Columbia University, New York, NY, USA

4 ² NASA Goddard Institute for Space Studies, New York, NY, USA

5 *Correspondence to:* Susanne E. Bauer: Susanne.E.Bauer@nasa.gov

6

7

8

9

10

11

12

13

14

15

16

17

18

19

20

21

22

23

24

25

26

27

28

29

30

31

32 **Abstract.** Fires affect the composition of the atmosphere and Earth’s radiation balance
33 by emitting a suite of reactive gases and particles. An interactive fire module in an Earth
34 System Model (ESM) allows us to study the natural and anthropogenic drivers, feedbacks,
35 and interactions of open fires. To do so, we have developed pyrE, the NASA GISS
36 interactive fire emissions module. The pyrE module is driven by environmental variables
37 like flammability and cloud-to-ground lightning, calculated by the GISS ModelE ESM,
38 and parameterized anthropogenic impacts based on population density data. Fire
39 emissions are generated from the flaming phase in pyrE (active fires). Using pyrE, we
40 examine fire occurrence, regional fire suppression, burned area, fire emissions, and how
41 it all affects atmospheric composition. To do so, we evaluate pyrE by comparing it to
42 satellite-based datasets of fire count, burned area, fire emissions, and aerosol optical
43 depth (AOD). We demonstrate pyrE’s ability to simulate the daily and seasonal cycles of
44 open fires and resulting emissions. Our results indicate that interactive fire emissions are
45 biased low by 32-42%, depending on emitted species, compared to the GFED4s
46 inventory. The bias in emissions drives underestimation in column densities, which is
47 diluted by natural and anthropogenic emissions sources and production and loss
48 mechanisms. Regionally, the resulting AOD of a simulation with interactive fire
49 emissions is underestimated mostly over Indonesia compared to a simulation with
50 GFED4s emissions and to MODIS AOD. In other parts of the world pyrE’s performance
51 in terms of AOD is marginal to a simulation with prescribed fire emissions.

52 **1 Introduction**

53 Open biomass burning (BB), the outdoor combustion of organic material in the
54 form of vegetation, occurs on every continent, with the exception of Antarctica, at a scale
55 observable from space. Open BB is perceived as a natural ecological process that has
56 been modulating the carbon cycle for more than 420 million years [*Scott and Glasspool,*
57 2006]. However, in practice, BB has been mediated by human activities for more than
58 100,000 years [*Bowman et al., 2009, 2011; Archibald et al., 2012*]. *Bellouin et al. (2008)*
59 estimated that at present, only about 20% of fires, compared to preindustrial times, are
60 natural. *Andreae (1991)* estimated that in the tropics, where about 85% of fire emissions
61 occur [*van der Werf et al., 2017*], only 10% of fires are natural. In the USA, government
62 records show that about 85% of fires are started by humans [*Balch et al., 2017*]. Humans

63 affect fires directly through ignition and suppression, and indirectly through man-made
64 changes to land surfaces and climate. According to *Hantson et al.* (2015), land-use
65 practices are the most important driver of human-fire interactions.

66 BB regimes are often classified based on ecosystem type like boreal, temperate,
67 and tropical forests, savanna and grassland, peat land, and agricultural fires [*Ichoku et al.*,
68 2012]. However, fire characteristics also vary between geographic regions of the same
69 ecosystem type; for example, boreal fires in Russia have very different intensity,
70 efficiency, and emissions than boreal fires in Canada [*Wooster and Zhang*, 2004]. *Ichoku*
71 *et al.* (2008) suggested an energy-based classification of open BB indicating fire intensity,
72 similar to hurricanes, using the radiative power of satellite-retrieved fires. Globally,
73 satellite retrievals show that on average about 350 Mha are burned annually [*Giglio et al.*,
74 2013; *Chuvieco et al.*, 2016], about 4% of the global vegetated area [*Randerson et al.*,
75 2012], an area similar to that of India. African fires contribute about 70% to the global
76 total burned area (BA), with about equal contributions from Northern Hemisphere Africa
77 (NHAF, Fig. 1) and Southern Hemisphere Africa (SHAF). The most flammable
78 ecosystem, globally and specifically in Africa, is the savanna [*Ichoku et al.*, 2008;
79 *Randerson et al.*, 2012; *Giglio et al.*, 2013], which in the tropics (23.5° N - 23.5° S) alone
80 is responsible for 62% (1341 TgC a⁻¹) of global carbon emissions (2200 TgC a⁻¹) [*van der*
81 *Werf et al.*, 2017]. Australian bushfires (grass and shrub) and South American savanna
82 fires are the third and fourth largest regional contributors, with BAs of about 50 Mha and
83 20 Mha annually, respectively. Globally, *Randerson et al.* (2012) estimated an additional
84 contribution of 120 Mha from small fires. The thermal anomalies used to identify those
85 fires, which are mostly associated with agricultural fires, are below the detection limit of
86 satellite-retrieved surface reflectance, and come with large uncertainties. Regionally,
87 small fires can have a significant contribution to BA. By adding the contribution of small
88 fires, burned area increases in Equatorial Asia (EQAS) by 157%, in Central America
89 (CEAM) by 143%, and in Southeast Asia (SEAS) by 90% [*Randerson et al.*, 2012]. This
90 highlights the regional importance of small agricultural fires to regional fire activity.
91 Forest fires, including small fires, contribute about 17 Mha annually to global BA, and
92 are dominant in Temperate North America (TENA), Boreal North America (BONA),
93 Boreal Asia (BOAS) and EQAS.

94 BB can exist when three conditions are met: fuel is available, fuel is combustible,
95 and ignition sources are present [*Schoennagel et al.*, 2004]. The coincidence of these
96 conditions is seasonal, making open BB an inherently seasonal phenomenon. The peak
97 month and duration of fire season are coupled to the seasonal cycle in precipitation,
98 especially in the tropics [*Giglio et al.*, 2006; *Hantson et al.*, 2017]. Precipitation and fire
99 activity are sensitive to natural modes of variability like El Niño Southern Oscillation
100 (ENSO). In particular, the Southern Hemisphere BB activity is strongly coupled to ENSO
101 [*Buchholz et al.*, 2018]. During an El Niño year regional BB emissions can be up to two
102 times higher than their regional average level, due to increased fire activity in tropical
103 rainforests [*van der Werf*, 2004; *Andela and Werf*, 2014; *Field et al.*, 2016; *Whitburn et*
104 *al.*, 2016].

105 Forest fires are either ignited on purpose, as part of forest management practices
106 [*Ryan et al.*, 2013], ignited by accident, as a by-product of the expansion of urban life to
107 the wildland interface [*Moritz et al.*, 2014; *Fischer et al.*, 2016; *Radeloff et al.*, 2018], or
108 ignited by lightning [*Díaz-Avalos et al.*, 2001]. Thus, fire activity is highly coupled to
109 trends in population density as increased population density at the wildland-urban
110 interface (WUI) increases the probability of fire [*Radeloff et al.*, 2018], while land
111 abandonment leads to shrub encroachment, and fuels fire activity [*Butsic et al.*, 2015].

112 Although BB emissions have high spatiotemporal variability, their impact on
113 atmospheric composition is significant [*Crutzen et al.*, 1979; *Seiler and Crutzen*, 1980;
114 *Crutzen and Andreae*, 1990]. BB emissions impact air quality [*Johnston et al.*, 2012,
115 2014, 2016; *Bauer et al.*, 2019], and climate [*Ward et al.*, 2012; *Lasslop et al.*, 2019].
116 Emitted pollutants include ozone precursors like methane ($\sim 49 \text{ Tg a}^{-1}$), carbon monoxide
117 ($\sim 820 \text{ Tg a}^{-1}$), and NO_x (mostly emitted as NO, $\sim 19 \text{ Tg a}^{-1}$) [*Andreae*, 2019]; the latter
118 two are also deleterious for health on their own. In addition to gaseous pollutants, BB
119 emits particulate matter (a total of $\sim 85 \text{ Tg a}^{-1}$) like primary emitted black carbon ($\sim 5 \text{ Tg}$
120 a^{-1}) and organic carbon ($\sim 36 \text{ Tg a}^{-1}$), as well as precursors of brown carbon, and
121 secondary organic and inorganic aerosols like non-methane volatile organic compounds
122 (NMVOC, $\sim 58 \text{ Tg a}^{-1}$), ammonia ($\sim 9.9 \text{ Tg a}^{-1}$), sulfur dioxide ($\sim 6 \text{ Tg a}^{-1}$), and NO_x
123 [*Andreae*, 2019]. Exposure to these pollutants at high concentrations or for a long period
124 of time can compromise the cardiorespiratory system and lead to death [*Lelieveld et al.*,

125 2015]. These pollutants, along with BB-emitted greenhouse gases (GHGs) like carbon
126 dioxide (CO₂; ~13,900 Tg a⁻¹) and nitrous oxide (N₂O; ~1.38 Tg a⁻¹), interact with
127 radiation, directly and indirectly. Fires are a net source of carbon dioxide only where
128 vegetation regrowth is inhibited, i.e. in deforested areas; otherwise BB is not viewed as a
129 source of CO₂ but as “fast respiration” [van der Werf *et al.*, 2017]. Absorbing black and
130 brown carbon [Lack *et al.*, 2012; Lack and Langridge, 2013; Laskin *et al.*, 2015], and
131 reflecting primary and secondary organic and inorganic aerosols interact with solar
132 radiation directly by scattering and absorbing radiation, and indirectly by modifying
133 clouds. The radiative properties of particles and their hygroscopicity are also influenced
134 by their mixing state [Bauer and Menon, 2012]. For example, when black carbon (BC) is
135 coated it becomes even more absorbing per unit mass [Bond and Bergstrom, 2006]. There
136 is evidence that smoke plumes can suppress or invigorate precipitation [Feingold *et al.*,
137 2001; Andreae *et al.*, 2004; Tosca *et al.*, 2015]. Aerosols impact cloud height and cover
138 by modifying the heat profile of the atmosphere and increasing the number of cloud
139 condensation nuclei. There are large uncertainties associated with aerosols’ impact on
140 climate. Modeling studies suggest that the aerosol effects from BB emissions overrides
141 the BB-GHG effect to a net negative radiative forcing [Mao *et al.*, 2013], with the
142 indirect effect of clouds dominating the forcing [Ward *et al.*, 2012]. The present day BB
143 forcing is estimated at -0.5-(-0.1)±0.05 Wm⁻² [Ward *et al.*, 2012; Mao *et al.*, 2013; Jiang
144 *et al.*, 2016; Landry and Matthews, 2016; Lasslop *et al.*, 2019].

145 The quantification of speciated BB emissions is challenging due to the fact that no
146 one fire is the same as another [Ito and Penner, 2005]. The composition of the resulting
147 smoke plume depends on the fuel type, burning conditions (i.e. flaming or smoldering),
148 fuel consumption, and on background chemistry. More complete combustion has a higher
149 fraction of oxidized species (e.g. CO₂ and NO_x) while smoldering fires release more
150 reduced species (e.g. CO, NH₃, NMVOCs). Globally, most fire emissions occur during
151 the active phase of the fire, with peat fires as the main exception [Andreae, 2019]. Thus,
152 emissions in different regions contribute different amounts of pollutants; Indonesia, for
153 example, is responsible for 8% of global carbon BB emissions, but 23% of methane BB
154 emissions [van der Werf *et al.*, 2017]. Emissions are sensitive to season and region. Even
155 within one region, like a boreal forest, emissions from crown fires differ from those from

156 ground fires. The amount of fuel consumed by a fire is highly variable and depends on
157 fuel load, density, moisture, vegetation type, and on environmental factors such as wind
158 speed, soil moisture and soil composition. Additional challenges relate to external forcing
159 like insect herbivory, mammal grazing, and manmade land fragmentation and
160 deforestation [*Schultz et al.*, 2008]. The quantification of BB emissions has an even
161 bigger importance during preindustrial times, where fire emission are identified as the
162 largest source of uncertainty for aerosol loading in Earth system models [*Hamilton et al.*,
163 2018]. BB emissions are a key quantity needed for quantifying the unperturbed-from-
164 humans background conditions of the atmosphere [*Carslaw et al.*, 2013].

165 Traditionally, fires are included in climate models using emission inventories
166 [*Lamarque et al.*, 2010; *van der Werf et al.*, 2010, 2017; *van Marle et al.*, 2017]. Some
167 models have the ability to simulate BB emissions interactively with a varying level of
168 complexity [*Thonicke et al.*, 2001; *Arora and Boer*, 2005; *Pechony and Shindell*, 2009; *Li*
169 *et al.*, 2012; *Lasslop et al.*, 2014; *Hantson et al.*, 2016; *Mangeon et al.*, 2016; *Rabin et al.*,
170 2017; *Zou et al.*, 2019]. On the one end of the spectrum, there are statistically-based
171 models, and on the other end there are detailed empirical and physical process-based
172 models. Statistical models are skilled at making predictions based on present-day
173 relationships between climate and fire (their training data). Process-based models
174 encapsulate the complex feedbacks within the climate system at various levels. They
175 combine physical processes such as fuel condition, cloud-to-ground lightning ignitions,
176 and wind-driven fire expansion. The most sophisticated models are coupled to dynamic
177 global vegetation models and directly connect fire-Earth system interactions through fuel
178 consumption (e.g. LPJ-GUESS-GlobFIRM, LPJ-GUESS-SIMFIRE-BLAZE (*Smith et al.*,
179 2001, 2014; *Lindeskog et al.*, 2013), and MC-Fire (*Bachelet et al.*, 2015; *Sheehan et al.*,
180 2015)). Some models also include simplified empirical relationships of anthropogenic
181 ignition and suppression, which, at present, are not understood in a dynamic process level.
182 State-of-the-art process-based fire models are well equipped to study the feedbacks
183 between the climate system and fires [*Hantson et al.*, 2016]. However, there is indication
184 that they lack accurate predictive capabilities, as they only partly capture trends in present
185 day observations. For example, satellite products show a global decrease in burned area
186 from about 500 Mha a⁻¹ in 1997 to 400 Mha a⁻¹ in 2013, a trend which fire models do not

187 capture [Andela *et al.*, 2017]. This trend is mostly driven by land fragmentation and
188 grazing practices over African savanna, highlighting the challenge of fire models to
189 account for the combined changes in climate, vegetation and socio-economic drivers
190 [Forkel *et al.*, 2019]. Though less accurate than observational datasets, when trying to
191 simulate individual fire events, fire models provide the unique advantage of linking the
192 atmosphere, biosphere and hydrosphere in a consistent way, a crucial step when studying
193 Earth System interactions. They are also able to predict fire during climate periods for
194 which we have no observational data available (e.g. preindustrial and future).

195 In this paper we present a new global fire module, pyrE, based on an improved
196 scheme of [Pechony and Shindell, 2009, 2010] with new capabilities. The pyrE module is
197 process-based, as it includes the two basic parameters of fuel availability and
198 combustibility, which are used to calculate active fires. It utilizes empirical relationships
199 with population density to account for the anthropogenic impact on fire ignition and
200 suppression. However, unlike most fire models where fire suppression is applied
201 uniformly across all regions [Rabin *et al.*, 2017], in pyrE fire suppression depends both
202 on population density and region. Additionally, pyrE uses active fires to derive emissions
203 in contrast to other fire models that use BA. The fire module is part of the NASA GISS
204 ModelE Earth System model, ModelE2.1 (an updated version based on Schmidt *et al.*
205 (2014)), and is described below.

206 **2 Model description**

207 pyrE, from the Greek word for fire (pyr, πυρ), is a global fire module within GISS
208 ModelE. It incorporates the active fire parameterization of Pechony and Shindell (2009,
209 2010), with the addition of fire spread and BA, following the Community Land Model's
210 (CLM) approach [Li *et al.*, 2012]. The module is a collection of physical processes like
211 flammability, natural ignition, fire spread, and fire emissions, and empirical processes
212 that include accidental ignition and suppression (Fig. 2). The climate model input
213 required, includes surface temperature, surface relative humidity (RH), precipitation,
214 surface wind speed, vegetation density and type, cloud-to-ground lightning frequency and
215 population density. Like many fire modules it lacks explicit intentional ignition (e.g. crop,
216 deforestation) and peat fires.

217 **2.1 Flammability**

218 Flammability is a parameter that indicates conditions favorable for fire occurrence
 219 [*Pechony and Shindell, 2009, 2010*]. It is a unit-less number that ranges between zero and
 220 one, and is calculated using vapor pressure deficit (*VPD*), monthly-accumulated
 221 precipitation, and vegetation density (*VD*).

222 *VPD*, an indicator of drought [*Seager et al., 2015; Williams et al., 2015*], is
 223 calculated via the Goff-Gratch equation [*Goff and Gratch, 1946; Goff, 1957*] using the
 224 saturation vapor pressure (e_s) and surface relative humidity (*RH*):

$$225 \quad VPD = e_s \left(1 - \frac{RH}{100}\right) \quad (1)$$

226 Where $e_{st} = 1013.245$ [*mb*] is the saturation vapor pressure at the boiling point
 227 of water and $e_s = e_{st} 10^{Z(T)}$ depends on temperature (*T*):

$$228 \quad Z(T) = a \left(\frac{T_s}{T} - 1\right) + b \cdot \log\left(\frac{T_s}{T}\right) + c \left(10^{d\left(1 - \frac{T_s}{T}\right)} - 1\right) + f \left(10^{h\left(\frac{T_s}{T} - 1\right)} - 1\right) \quad (2)$$

229 With the coefficients: $a = -7.90298$; $b = 5.02808$; $c = -1.3816 \cdot 10^{-7}$; $d =$
 230 11.344 ; $f = 8.1328 \cdot 10^{-3}$; $h = -3.49149$ [*Goff and Gratch, 1946*], and $T_s =$
 231 373.16 [$^{\circ}K$] (water boiling point temperature).

232 The precipitation dependence of flammability is in the form of an inverse
 233 exponential (Following [*Keetch and Byram, 1968*]):

$$234 \quad f(R) = \exp(-c_R R) \quad (3)$$

235 Where *R* is the surface rain rate in mm per day and $c_R = 2$ [*day/mm*] is an
 236 empirical constant [*Pechony and Shindell, 2009*].

237 Vegetation density (*VD*) is taken as the normalized leaf area index (*LAI*) in the
 238 land fraction of a grid cell, varying between 0 for no vegetation and 1 for dense
 239 vegetation.

240 We modified the original calculation proposed by [*Pechony and Shindell, 2009*]
 241 by calculating flammability only for the fraction of the model's grid cell that is not
 242 burned from previous fires. The flammability *F* at a time step *t* in a grid cell (*i, j*) is:

$$243 \quad F(t) = 10^{Z(T(t)_{i,j})} \left(1 - \frac{RH(t)_{i,j}}{100}\right) VD(t)_{i,j} \left(1 - \frac{BA(t)_{i,j}}{LA_{i,j}}\right) \exp(-c_R R(t)_{i,j}) \quad (4)$$

244 Where $LA_{i,j}$ is the total land area (*LA*) in the grid cell (*i, j*).

245 2.2 Ignition

246 Natural and anthropogenic ignition varies in space and time, and is necessary for
247 the calculation of active fires. If ignition is zero, the resulting number of active fires will
248 be zero, independent of flammability. Natural ignition is in the form of cloud-to-ground
249 lightning frequency, which is interactively calculated in ModelE2.1 [*Price and Rind*,
250 1992, 1993]. The parameterization of anthropogenic ignition follows *Venevsky et al.*
251 (2002) and is based on the assumption that in sparsely populated regions people interact
252 more with the natural environment, thus increasing the potential for ignition. The
253 parameterization uses population density data and empirical scaling factors, as described
254 by *Pechony and Shindell* (2009), and does not include intentional ignition. The number of
255 anthropogenic accidental ignitions per km² per month is:

$$256 \quad I_A = k(PD)PD\alpha \quad (5)$$

257 Where PD is the population density; $k(PD) = 6.8PD^{-0.6}$ represents the varying
258 anthropogenic ignition potentials as a function of population density; $\alpha = 0.03$ is the
259 number of potential ignitions per person per month. Coefficients are taken following
260 *Pechony and Shindell* (2009) and *Mangeon et al.* (2016) which utilized correlation
261 calculations done by *Venevsky et al.* (2002).

262 **2.3 Suppression**

263 A first-order approximation of the impact of population density on explicit fire
264 suppression was proposed by *Pechony and Shindell* (2009). According to that
265 parameterization, more fires are suppressed in densely populated areas compared to
266 sparsely populated areas, regardless of ignition source. Specifically, suppression varies
267 from 5% to 95% of fires. However, fire management is a region-specific practice, which
268 depends on cultural norms and economic capabilities. For example, fire suppression in
269 the United States of America (USA) is a common practice (*Parisien and Moritz*, 2009;
270 *Marlon et al.*, 2012) while active fire suppression in most parts of Africa is not
271 commonly practiced. Most fire suppression in Africa is an indirect byproduct of changes
272 in land surface properties through grazing and fragmentation (*Archibald*, 2016). Hence,
273 we modified the simplistic approach suggested by *Pechony and Shindell* (2009), guided
274 by the results presented in Sect. 5.1.1 to better match with observed fire activity at
275 specific regions. Our initial analysis showed that with the original *Pechony and Shindell*
276 (2009) suppression scheme fire activity is overestimated in the TENA and MIDE regions

277 while being underestimated in NHAf and SHAF. Following these initial results a series
 278 of sensitivity simulations were conducted with varying values of suppression coefficients.
 279 The final values were chosen in a heuristic manner that improved the simulations yet did
 280 not over-fit them to the observations, similarly to *Pechony and Shindell (2009)* and other
 281 fire parameterization, due to the lack of appropriate global data.

282 We use the complement of the fraction of suppressed fires that is the fraction of
 283 non-suppressed fires, f_{NS} :

$$284 \quad f_{NS} = \begin{cases} 0.2 \exp(-0.05PD), & \text{USA and MIDE} \\ 1, & \text{Africa} \\ 0.05 + 0.9 \exp(-0.05PD), & \text{Elsewhere} \end{cases} \quad (6)$$

285 2.4 Active fires

286 Active fires are a key metric used to drive burned area and fire emissions in pyrE.
 287 The number of fires in a time step per km² is calculated as the product of flammability,
 288 sum of natural and anthropogenic ignition, and suppression [*Pechony and Shindell, 2009*]
 289 (Fig. 2):

$$290 \quad N_{fire}(t)_{i,j} = F(t)_{i,j} \cdot (I_N(t)_{i,j} + I_A(t)_{i,j}) \cdot f_{NS}(t)_{i,j} \quad (7)$$

291 2.5 Burned area (BA)

292 We adopted the process-based approach of *Li et al. (2012)* to calculate fire spread
 293 and burned area. The burned area in grid cell (i, j) at a model time step t is the product of
 294 active fires and the weighted average over plant functional types (PFTs) of the area
 295 burned by one fire:

$$296 \quad BA_{i,j} = N_{fire}(t)_{i,j} \cdot \sum_v a_{i,j,v} \cdot f_{i,j,v} \quad (8)$$

297 Where $f_{i,j,v}$ is the fractional area covered by plant functional type v , and the
 298 burned area of a single fire $a_{i,j,v}$ is assumed to have an elliptical shape (Fig. 3). Wind
 299 speed, surface relative humidity, and vegetation type control the eccentricity of the
 300 ellipsoid that represents the burned area of a single fire (based on *van Wagner (1969)*):

$$301 \quad a_{i,j,v} = \frac{\pi ROS^2 \tau^3}{4LB} \left(1 + \frac{1}{HB}\right)^2 \quad (9)$$

302 Where ROS is the rate of fire spread, LB is the length-to-breadth ratio, and HB is
 303 the head-to-breadth ratio. The stronger the wind, the more eccentric the ellipse, i.e. the
 304 bigger the length-to-breadth ratio:

$$305 \quad LB = 1 + 10 \cdot (1 - \exp(-0.06W)) \quad (10)$$

306 Where W is the surface wind speed in m s^{-1} .

307 Strong winds also increase the head to back ratio; the ratio of the downwind
308 spread compared to the upwind spread:

$$309 \quad HB = \frac{LB + \sqrt{LB^2 - 1}}{LB - \sqrt{LB^2 - 1}} \quad (11)$$

310 The rate of spread (ROS) of a fire is a function of vegetation type, wind speed,
311 and atmospheric and soil moisture:

$$312 \quad ROS = ROS_{max} \cdot gW \cdot f_{RH} \cdot f_{\theta} \quad (12)$$

313 ROS_{max} is the maximum fire spread rate. Following *Li et al.* (2012), we set it to
314 0.2 m s^{-1} for grasses, 0.17 m s^{-1} for shrubs, 0.15 m s^{-1} for needle leaf trees, and 0.11 m s^{-1}
315 for other trees. *Li et al.* (2012) estimated the fire spread coefficients to be on the lower
316 range of observed ROS, but are yet higher than the global value of 0.13 m s^{-1} suggested
317 by *Arora and Boer* (2005).

318 The limit of the fire spread is set by:

$$319 \quad gW = \frac{2LB}{1 + \frac{1}{HB}} g0 \quad (13)$$

$$320 \quad \text{Where } g0 = \frac{1 + HB_{max}^{-1}}{2LB_{max}} \approx 0.05$$

321 f_{RH}, f_{θ} are the dependencies of fire spread on RH and root zone soil moisture:

$$322 \quad f_{RH} = \begin{cases} 1 & RH \leq RH_{low} \\ \frac{RH_{up} - RH}{RH_{up} - RH_{low}} & RH_{low} < RH < RH_{up} \\ 0 & RH \geq RH_{up} \end{cases} \quad (14)$$

323 Following *Li et al.* (2012), we set $RH_{low} = 30\%$, $RH_{up} = 70\%$ and $f_{\theta} = 0.5$
324 as ModelE2.1 does not simulate prognostic root zone soil moisture.

325 2.6 Emissions

326 Trace gas and aerosol emissions are generated during the active phase of the fire
327 and are calculated as the product of the simulated active fires and emission factors
328 ($EF_{s,v}$) and are a function of PFT (denoted by v) and chemical specie (denoted by s). The
329 use of active fires to derive emissions is driven by the extremely rudimentary
330 representation of the terrestrial biosphere in ModelE, under which interactive fuel
331 consumption cannot be calculated. The emissions per grid cell (i, j) of specie s at a
332 model time step t are calculated by:

333
$$E_{i,j,s}(t) = N_{fire}(t)_{i,j} \cdot \sum_v EF_{s,v} \cdot f_{i,j,v} \quad (15)$$

334 Where $E_{i,j,s}(t)$ is the emissions flux rate in $\text{kg m}^{-2} \text{s}^{-1}$, $N_{fire}(t)_{i,j}$ are the number
335 of active fires, $EF_{s,v}$ are the offline emission factors, and f_v is the fractional area of that
336 PFT in the grid cell.

337 Emission factors describe the PFT-specific speciated mass (in kg) of the smoke,
338 normalized per fire (Table 1). Emission factors were calculated offline using ModelE2.1
339 PFTs, annual mean global MODIS Terra fire count, and GFED4s emissions from the
340 period of 2003-2009. Our technique, known as multivariate curve fitting, matched the
341 emissions within the PFT fraction of the grid cell with the respective fire count. We
342 correlated a time series of GFED4s emissions with a time series of MODIS fire count for
343 each modeled PFT in a grid cell. Our settings included statistical (Poisson) weighting of
344 the GFED4s emissions (1 over emissions) and a uniform initial estimate of $100,000 \text{ kg m}^{-2} \text{ s}^{-1}$
345 per fire per PFT. This calculation resulted with a specific emission factors per PFT
346 (Table 1).

347 **2.7 Implementation within ModelE**

348 ModelE2.1 can be used with either GFED4s prescribed fire emissions or
349 interactive pyrE emissions. The pyrE module generates emissions at every model time
350 step with ESM-simulated climate as a driver. Flammability is calculated only in the
351 fraction of grid cells with natural vegetation. It is driven by the simulated surface RH,
352 surface temperature, monthly accumulated precipitation, and LAI. LAI is calculated by
353 Ent [Kim *et al.*, 2015], the Terrestrial Biosphere Model component of ModelE2.1, and is
354 currently derived from 2005 MODIS LAI data [Tian *et al.*, 2002a, 2002b]. Cloud-to-
355 ground lightning, calculated by ModelE2.1, is used as the natural ignition source. Most
356 ESMs have low skill in reproducing flash rate distributions [Murray, 2016], and the GISS
357 model is no exception. A qualitative comparison with the World Wide Lightning
358 Location Network (WWLN) (not presented here) showed that modeled cloud-to-ground
359 lightning, which makes up only about 30% of total lightning, is biased high in ModelE2.1.
360 We decided to use a simple scaling factor of 0.1 in the calculation of natural ignition to
361 better match observed flash rates, as improving the lightning parameterization is beyond
362 the scope of this study.

363 All fire-related parameters like flammability, active fires, burned area, and fire
364 emissions are recalculated in every model time step (30 min) with memory only of the
365 burned area in the previous time step. We could not extend the “fire memory” past the
366 previous time step due to limitations related to ModelE’s terrestrial biosphere module.
367 However this is a reasonable application, given that the climate inputs we use for fire
368 calculations such as monthly accumulated precipitation, surface RH and temperature
369 don’t change significantly between each time step. The fire module’s impact on the Earth
370 system is currently only through interactive emissions. Albedo, carbon stocks and LAI
371 are not modified by pyrE.

372 The modeling approach presented in this paper provides a good reproduction of
373 the seasonality compared to satellite retrievals (see Results section). However, the
374 simulated magnitude of active fires and burned area was too small compared to satellite
375 retrievals and required the use of a scaling factor, a common practice among other fire
376 models [*Pfeifer et al.*, 2013; *Hantson et al.*, 2016; *Mangeon et al.*, 2016; *Zou et al.*,
377 2019]. To calibrate the global modeled active fires to MODIS retrievals, we used a global
378 scaling factor of 30 for all active fires. A similar approach was taken by *Pechony and*
379 *Shindell* (2009). We scaled burned area by a factor of 250 to reach the magnitude of
380 GFED4s. Nevertheless, even with this large correction factor, burned area, which
381 accounts for a small fraction of the grid cell that is able to burn, has a very minor impact
382 on fire activity and fire emissions as its only impact to fire activity is through
383 flammability.

384 **3 Model configuration**

385 We used ModelE2.1 with a spatial resolution of 2° in latitude by 2.5° in longitude,
386 40 vertical layers and a model top at 0.1 hPa. The vegetation component of ModelE2.1 is
387 the Ent Terrestrial Biosphere Model (Ent TBM), which is coupled with the land use/land
388 cover data in the model [*Kim et al.*, 2015]. Ent prescribes leaf area index (LAI) for 14
389 plant functional types (presented in Table 1) derived from MODIS 2005 data (cover and
390 biome types [*Friedl et al.*, 2010]; LAI [*Tian et al.*, 2002a, 2002b]), historical crop cover
391 [*Pongratz et al.*, 2008], and vegetation heights from [*Simard et al.*, 2011].

392 In this study we show results from runs of ModelE2.1 coupled to the aerosol
393 microphysical scheme MATRIX (Multiconfiguration Aerosol TRacker of mIXing state)

394 [Bauer *et al.*, 2008]. MATRIX simulates aerosol formation, condensation and
395 coagulation, calculates the size distribution of aerosols and tracks their mixing state. Sea
396 salt, dust, and dimethyl sulfide (DMS) emissions were calculated interactively, driven by
397 the simulated climate, while other natural and anthropogenic fluxes, except for fires, were
398 prescribed from the CEDS (Community Emissions Data System) inventory [Hoesly *et al.*,
399 2018].

400 In the following, we will present a simulation with pyrE turned on, generating
401 interactive fire emissions, and a simulation with pyrE turned off, using prescribed 2005
402 climatological (interpolated 2000-2010) GFED4s emissions instead. Also, we will
403 discuss sensitivity studies using two simulations where pyrE generates interactive fire
404 emissions but suppression is changed from a global parameterization to a regional one.
405 Prescribed climatological monthly varying mean (1996-2004) sea surface temperature
406 and sea ice thickness and extent were used as boundary conditions [Rayner *et al.*, 2003].

407 **4 Dataset**

408 Most of the data below are based on a composite of level 3 Aqua and Terra
409 Moderate-resolution Imaging Spectro-radiometer (MODIS) Collection 5.1 data [Giglio *et*
410 *al.*, 2003b; Giglio, 2013], unless otherwise stated. Aqua and Terra are sun-synchronous,
411 near-polar orbiting satellites with a global continuous record of more than 15 years; Aqua
412 was launched in May 2002 and Terra in December 1999. Aqua's overpass time is
413 1:30AM and 1:30PM local, and Terra's overpass time 10:30AM and 10:30PM local, and
414 their period is between one to two days. All reference data used in this study are
415 interpolated and re-gridded to the resolution of ModelE2.1.

416 **4.1 Population density**

417 Gridded population density (PD) that drives both anthropogenic ignition and fire
418 suppression is based on historical data for years prior to 2010 [Klein Goldewijk *et al.*,
419 2010]. PD has a time resolution of 10 years and is interpolated in between.

420 **4.2 Fire count**

421 To detect fires, MODIS uses brightness temperatures (thermal anomaly) derived
422 from two channels [Justice *et al.*, 2002; Giglio *et al.*, 2006]. In our study we used the
423 monthly cloud-corrected fire count (CloudCorrFirePix) climate model grid data
424 (MYD14CMH, MOD14CMH). One single fire might include multiple fire pixels. The

425 spatial resolution of the data is 0.5° . Static, persistent hot spots are excluded from this
426 product [Giglio, 2013]. Because of its non-uniform spatial and temporal sampling, raw
427 MODIS data are biased high at high latitudes [Giglio *et al.*, 2003a, 2006]. The product
428 we used is corrected for the multiple satellite overpasses, the missing data, and variable
429 cloud cover. Cloud cover hinders MODIS retrievals. The active fires in the product we
430 used are normalized to the fraction of cloud cover in a pixel. In highly cloudy pixels, the
431 product is set to zero. The local time of retrieval matters for fire detection, as fires are
432 driven by the daily cycle in solar heating. The largest number of active fires is detected
433 during daytime, with an order of magnitude difference between daytime detections and
434 nighttime detections [Ichoku *et al.*, 2008]. Thus, differences are evident between the
435 Aqua and Terra retrievals. This motivated us to use data from the two satellites in our
436 analysis. We calculate and utilize climatological monthly means from the period 2003-
437 2016.

438 **4.3 Burned area**

439 We used burned area from the Global Fire Emissions Database (GFED) version
440 4s that includes small fires [van der Werf *et al.*, 2010, 2017; Randerson *et al.*, 2012;
441 Giglio *et al.*, 2013]. The GFED4s inventory is based on multi-sensor MODIS data,
442 involving both reflectance and thermal anomalies measurements from Aqua and Terra.
443 Retrievals must be free from cloud contamination and free from active fires within the
444 500 m MODIS grid cell. First, to generate the GFED4s data, MODIS burned area
445 collection 5.1 data (MCD64A1 product) are aggregated to a 0.25° grid. Then, burned area
446 from small fires is added. The burned area of small fires is statistically estimated using
447 active fires detected by MODIS (a composite of both Aqua and Terra). In this study we
448 use climatological monthly means of burned area from the period 2003-2016.

449 **4.4 Biomass burning emission inventory**

450 GFED4s emissions are derived from the multiplication of burned area and fuel
451 consumption [van der Werf *et al.*, 2010, 2017]. As such, they have the same spatial and
452 temporal resolution as burned area, of 0.25° by 0.25° and a month. Fuel consumption is
453 calculated using an estimation of fuel loss and combustion completeness, which are
454 calculated using MODIS-based metrics such as differences in normalized burned area
455 (dNBR), normalized vegetation index (NDVI), and land surface temperature (LST). The

456 satellite-based data are used as input to the Carnegie–Ames–Stanford Approach (CASA)
457 biogeochemical model [Randerson *et al.*, 1996] to calculate the dry matter burned. Then,
458 emission factors [Andreae and Merlet, 2001; Akagi *et al.*, 2011] are applied to convert
459 the dry matter burned to PFT-specific speciated gas and aerosol phase emissions. Kaiser
460 *et al.* (2012) and Pan *et al.* (2020) showed that there are regional biases in older and
461 current versions of GFED; being especially biased low in the Southern Hemisphere
462 compared to AERONET aerosol optical depth (AOD). In order to eliminate the strong
463 interannual BB variability, our analysis used GFED4s mean climatological data of 2000-
464 2010.

465 **4.5 Fire regions**

466 The analysis we present below is based on the widely used fire regions (Fig. 1) as
467 defined by GFED [Giglio *et al.*, 2006; van der Werf *et al.*, 2006]. The regions are defined
468 based on climate and fire regimes, and are widely used as basis regions for global fire
469 studies.

470 **4.6 Aerosol optical depth**

471 The impact of fire emissions on atmospheric composition is investigated by
472 comparing monthly Aqua and Terra MODIS retrievals of AOD at 550nm [Remer *et al.*,
473 2005; Platnick *et al.*, 2015]. AOD describes the entire atmospheric column-integrated
474 extinction of aerosols. MODIS AOD data are a useful tool in the study of simulated BB
475 plumes [Voulgarakis and Field, 2015; Johnson *et al.*, 2016; Bauer *et al.*, 2019]. The
476 AOD data we used has a 1° spatial resolution. The monthly mean data (MYD08_M3 and
477 MOD08_M3 products) have been averaged over the period 2003–2007 to create monthly
478 climatologies centered around the year 2005. The AOD product we use includes
479 improvements made via the Dark Target algorithm [Kaufman *et al.*, 1997], which was
480 developed particularly for retrievals over dark vegetated surfaces [Wei *et al.*, 2019].
481 However, the algorithm fails at retrieving valid AOD data over bright surfaces like desert
482 areas [Levy *et al.*, 2013], which we discard. Here we use collection 6.1 data.

483 **5 Results and discussion**

484 **5.1 Fire activity**

485 **5.1.1 Regional suppression**

486 First we want to demonstrate how the parameterization with regionally-dependent
487 fire suppression improves the simulation of fire activity compared to the original
488 simplified global fire suppression proposed by *Pechony and Shindell* (2009) (Fig. 4). Our
489 goal was to improve the fire parameterization in regions where the seasonality was
490 captured in timing but not in magnitude. We propose regional modifications to Africa
491 (NHAF, SHAF), a region that drives global fire activity, and had a distinct mismatch in
492 active fires compared to satellite retrievals. Originally, over NHAF the fire seasonality
493 was too flat, while over SHAF it matched MODIS-Terra, but was orders of magnitude
494 smaller than MODIS-Aqua. Since fire suppression for open BB is not commonly
495 practiced in rural Africa, eliminating it over NHAF and SHAF helped resolve the
496 seasonal cycle (Fig. 4 and Eq. 6). The two other regions we modified are TENA and
497 Middle East (MIDE). Over both of those regions the simulated fire seasonality was too
498 strong. Increasing fire suppression over MIDE and TENA greatly improved our
499 simulations compared to MODIS retrievals.

500 The pyrE module is skilled at capturing the fire seasonality in regions identified
501 by *Forkel et al.* (2017) as controlled by temperature and wetness (climate controls), like
502 Southern Hemisphere South America (SHSA) (Fig. A1). However, there are regions that
503 our parameterization does not simulate well, mainly due to the fact that the fire activity
504 there is driven by land use practices and intentional fire ignitions, which pyrE does not
505 resolve. For example, in TENA we are missing the spring peak of agricultural fires.
506 Similarly, over Europe and Boreal Asia (Fig. A1) we are missing the winter and spring
507 fires associated with intentional ignition [*Dwyer et al.*, 2000; *Ganteaume et al.*, 2013].
508 Other regions where the seasonality is not well captured, likely due to the fact that it is
509 driven by intentional ignitions, include Central America, Northern Hemisphere South
510 America, Central Asia, Southeast Asia, and Equatorial Asia. Over Australia, the model
511 captures neither the magnitude nor the timing of the BB seasonality. This is in part due to
512 the model's poor performance of the simulated cloud-to-ground lightning ignitions in that
513 region (not shown).

514 In all simulations going forward we used the regional suppression scheme.

515 **5.1.2 Daily cycle**

516 We looked at the active fires' daily cycle to see if it can explain the differences
517 between Aqua, Terra, and the model. The monthly mean fire count detected by Aqua and
518 Terra is expected to be different due to their different overpass times. In Fig. 5, pyrE
519 simulates a distinct daily cycle in active fires in different locations. The simulated daily
520 cycle is most strongly controlled by the simulated daily cycle in flammability (not
521 presented here), matching the daily solar cycle. pyrE's ability to resolve a daily cycle of
522 fire activity highlights the dynamic nature of a process-based fire model.

523 Using 30-minute simulation output, we sampled all surface grid cells at the
524 daytime overpass time of MODIS Terra, 10:30am local time, and MODIS Aqua, 1:30pm
525 local time. We focused on the daytime overpass time of Terra and Aqua since about 95%
526 of active fire detections occur then [*Ichoku et al.*, 2008]. Our results in Fig. 6 and Fig. 7
527 indicate that, globally, simulated active fires sampled at daytime overpass are biased high
528 compared to MODIS retrievals from the respective satellite, for much of the year. On a
529 global annual mean, the active fires of the model sampled in daytime Terra overpass time
530 are higher than MODIS Terra by 45%, while the active fires of the model sampled in
531 daytime Aqua overpass time are higher than MODIS Aqua by 13%. However, this
532 behavior differs by region and maximizes in NH sub-Saharan Africa and SH central
533 Africa. The simulated fire activity is biased low compared to MODIS retrievals along the
534 coast of west Africa, in eastern southeast Asia and Australia. When simulated monthly
535 mean active fires values are in the range of Terra and Aqua (Fig. 4, A1), they are in fact
536 biased high, given the bias due to the overpass time of the satellite. Considering that the
537 actual number of active fires is likely higher than the number retrieved by MODIS, as
538 cloud contamination is decreasing its detection efficiency, it is conceivable that a model
539 weakly high-biased compare to the satellite retrievals is realistic. All results presented
540 later were not sampled according to a satellite overpass time, but instead were averaged
541 over the whole length of the day.

542 **5.2 Burned area**

543 The simulated burned area is biased low compared to the GFED4s inventory (Fig.
544 8, A2). The total annual simulated burned area (10-year climatological mean) is 380 Mha
545 while GFED4s burned area (mean of 2003-2016) is 460 Mha. However, this behavior is
546 region-specific. The simulated burned area is lower compared to GFED4s over northern

547 hemisphere Africa, particularly in November-December, over central and equatorial Asia,
548 and over Australia. The simulated burned area (Fig. 8, A2) reflects the spatial distribution
549 and seasonality of simulated active fires (Fig. 8, A1). GFED4s burned area and MODIS
550 fire count do not always have the same seasonality, for example during October-
551 December. During this season the satellite-retrieved fires produce a higher burned area
552 relative to other seasons. The fire activity driving this behavior occurs in the NHAF
553 savanna, and northern hemisphere South America. In those regions and times of the year
554 the normalized mean bias of modeled burned area is at least twice the size of the
555 normalized mean bias of active fires, e.g. in NHAF a bias of 6.5 for burned area and 1-3
556 for active fires, depending on the MODIS satellite. This implies that for every fire
557 modeled in these regions and season a smaller area is simulated to burn compared to the
558 reference datasets.

559 Why is the burned area per fire relationship in simulations much weaker than it is
560 in the reference datasets? Two contributing factors are: prescribed PFT and simulated
561 wind. The prescribed PFT distribution present in the model is rudimentary; it is
562 comprised of 11 flammable vegetation types (Table 1). As for surface winds, the
563 simulated wind patterns driving burned area are averaged over a coarse grid cell
564 ($2^\circ \times 2.5^\circ$). Simulated wind does not represent sub-grid scale processes and is not fueled
565 by the fire's energy, which is likely contributing to an underestimation of the spread of
566 burned area. However, though wind directly impacts burned area, it does not play a major
567 role in the distribution of simulated fires, since burned area itself has a minor impact on
568 fires through flammability due to its small percentage in a grid cell. At most burned area
569 reaches less than 18% of the naturally vegetated fraction of a grid cell, and is on average
570 less than 1%.

571 **5.3 Emissions**

572 Due to limitations in the current capabilities of the simulated terrestrial biosphere
573 in ModelE, emissions are generated from active fires, similar to the approach of *Pechony*
574 *and Shindell* (2009, 2010) and *Pechony et al.* (2013). The main source regions for fire
575 emissions are NHAF, EQAS, SHSA, and SHAF. Emissions are well simulated over
576 SHSA and SHAF (Fig. A3-A5), both in terms of timing of the seasonality and in
577 magnitude. The main regions where simulated emissions are lower than GFED4s are

578 NHAF and EQAS, mainly Indonesia (Fig. 8, A3-A5). However, more generally,
579 simulated gaseous and particulate emissions are globally biased low compared to
580 GFED4s emissions (Table 2). To a lesser degree, simulated fire emissions are also
581 weaker compared to GFED4s in the boreal regions (Fig. A3-A5). The contribution from
582 these regions to the global total is an order of magnitude smaller compared to the main
583 source regions.

584 The weaker emissions compared to GFED4s are responding to the following inputs:
585 offline emissions factors, lack of crop and peat fires, LAI, and prescribed PFTs. The
586 emission factors that generate fire emissions are derived using multivariate statistical
587 analysis. Though we used seven full years (2003-2009) of data to derive the factors, it
588 might have generated biases in emissions. Areas that burn annually are properly sampled,
589 but areas that have a fire cycle that is longer than a seven year might be biased high or
590 low, depending on whether they were included in the training dataset or not. Also, crop
591 and peat fires are not explicitly included in the simulated emissions, as intentional
592 ignition is not parameterized in pyrE. Specifically, fires are not applied to the crop fraction
593 of a grid cell, and peat surfaces are not included in the PFTs. However, our method of
594 deriving the offline emission factors uses MODIS fire count and GFED4s emissions, and
595 does not distinguish between intentional and accidental fires. Hence, intentional fires are
596 indirectly accounted for in the global sum. However, this indirect inclusion of intentional
597 fires does not necessarily add missing fire emissions in the correct locations. The LAI in
598 Ent, ModelE's DGVM, is based on 2005 MODIS retrievals. Though we cannot estimate
599 the role that the lack of interactive LAI plays, it is certainly not optimal, neither for fire
600 activity simulation, nor for fire emissions that are derived from active fires. Unlike
601 simulated active fires, simulated fire emissions are strongly tied to the map of PFTs. The
602 offline emission factors are based on prescribed PFTs, and the interactive emissions
603 themselves are applied according to the sub-grid PFT distribution. The prescribed PFT
604 distribution present in the model might be different than reality, and those differences
605 affect emissions. In the model, the PFTs in areas where emissions are biased high
606 compared to GFED4s there is a high percentage (>50%) of the following PFTs:
607 evergreen broadleaf trees (Amazon, central Africa), cold broadleaf trees (northeast
608 America, Europe), and drought broadleaf trees (central Africa and northern India). In

609 EQAS, a region with biased low simulated emissions, close to 100% of the prescribed
610 PFTs is evergreen broadleaf trees, which in reality is replaced by crops. The biased low
611 emissions in EQAS are very likely tied to the lack of prescribed peat PFT. In areas with
612 biased low emissions modeled PFTs are mainly (>50%) c4 grass (NHAF, Australia),
613 deciduous needle leaf trees (boreal regions), and arid shrubs (S Africa, Australia).

614 **5.4 Composition**

615 **5.4.1 Column load**

616 In order to quantify how the model skill changes with the inclusion of pyrE
617 instead of prescribed emission inventory data in ModelE2.1, we compare a simulation
618 with interactive fires to a simulation with prescribed BB sources. Though emissions are
619 mostly biased-low compared to GFED4s, this behavior is less evident in the column
620 density (Fig. 9). For most BB emitted species, the simulation with interactive fires has
621 lower column densities than the simulation with prescribed emissions (Table 2) with a
622 bias ranging from -6.3-0.5% for gaseous species, -4.8% for black carbon and -16% for
623 organic aerosol. However, the column densities are only partly driven by fire emissions,
624 as those make up less than 35% of total global emissions of either CO, organic aerosol,
625 and black carbon emissions. Non-emissions production-and-loss mechanisms also impact
626 column densities. Having a weak global impact on composition does not imply that
627 regionally fires are not important.

628 The difference in column densities between the two simulations is greatest over
629 north sub-Saharan Africa, Indonesia, and the boreal regions. The behavior is region-
630 specific, and some regions like central Africa and northern hemisphere South America
631 have higher column densities compared to the simulation with prescribed emissions. The
632 differences between the two simulations are more prominent for organic aerosol than any
633 of the other species (Fig. 9, Table 2), while the differences in the spatial distribution of
634 CO are marginal.

635 **5.4.2 Aerosol optical depth (AOD)**

636 In Fig. 10 we compare climatologically-simulated clear-sky AOD with MODIS
637 AOD (Aqua) for January, April, July, and October. The conclusions from Terra products
638 are similar to Aqua's, and will not be presented here, for brevity. In a regional
639 perspective, simulated AOD is able to reproduce the seasonality and spatial distribution

640 of MODIS-retrieved pollution over west and central Africa, east and southeast Asia, and
641 the Arabian sea. The simulations of ModelE2.1 has higher AOD compared to MODIS
642 over the tropical eastern Pacific, an artifact due to the model's skill in simulating
643 stratocumulus cloud decks, which have been improved in a newer version of the ESM
644 (ModelE3).

645 Model performance as a function of interactive versus offline fire emissions is
646 similar in terms of AOD (Fig. 11). Both simulations have persistently lower (0-30%)
647 AODs over central Africa and central South America compared to MODIS. The locations
648 with an outstanding difference in performance between the simulations are in central sub-
649 Saharan Africa in January and July, and over a small area in Indonesia (Kalimantan)
650 during October. In January over central sub-Saharan Africa the simulation with pyrE has
651 AOD values (NHAF regional mean AOD of 0.26) closer to MODIS (NHAF regional
652 mean AOD of 0.2) than a simulation with prescribed fire emissions (NHAF regional
653 mean AOD of 0.33), while in July it is the simulation with pyrE (NHAF regional mean
654 AOD of 0.53) that is more biased high than the prescribed one (NHAF regional mean
655 AOD of 0.46). Over EQAS in October the simulation with prescribed fires has an AOD
656 of ~0.28 while the simulation with pyrE has an AOD of ~0.18. AOD in this region is
657 sensitive to peat fires, which are not included in ModelE, strongly impacting pyrE's
658 results. Globally, mean AOD simulated with interactive fire emissions is 0.142 while
659 mean AOD simulated with prescribed fire emissions is 0.146. The fact that pyrE has a
660 marginal performance in climatological runs when compared against a simulation with
661 the more accurate offline emissions is a strong indication that it is a robust module that
662 can be used with confidence at time periods where offline emissions are not available.

663 Finally, we demonstrate the contribution of BB emissions to total clear-sky AOD
664 by comparing the simulations with both prescribed and interactive fire emissions to a
665 simulation that has no fire emissions at all (Fig. 12). In the simulation with prescribed fire
666 emissions, clear sky AOD is on average 10% higher than it is in a simulation with no fire
667 emissions. In a simulation with pyrE clear sky AOD is about 7.5% higher than it is in a
668 simulation with no fire emissions. The impact of BB emissions on AOD is most
669 pronounced in the source regions of Africa and the Amazon. In those regions the
670 difference in AOD varies between 0.15-0.3. It is important to note that the differences in

671 AOD are not only due to impact of BB emissions, but also reflect climate variability,
672 which impacts aerosol lifetime and interactive dust emissions.

673 **6 Conclusions**

674 The development of pyrE allowed us for the first time to interactively simulate
675 climate and fire activity with GISS-ModelE2.1. The pyrE module, which is based on a
676 the fire parameterizations of *Pechony and Shindell (2009)*, was expanded to include fire
677 spread and burned area, following the approach of *Li et al. (2012)*. This study set out to
678 simulate the climatology of fires, and not individual fire events. Like only a few other fire
679 models [*Zou et al., 2019*], pyrE was developed with consideration of regional behavior.
680 The new fire suppression scheme depends on population density, but also on geographic
681 regions. The new scheme reflects more intense fire suppression in the USA and Middle
682 East, and revokes fire suppression in Africa, which improved the fire activity seasonality
683 simulated by pyrE compared to satellite retrievals. Active fires' seasonality is well
684 simulated in the fire source regions: the Amazon, SH Africa, and NH Africa, with the
685 exception of being biased low compared to MODIS during November-December. This is
686 due to the lack in parameterization of intentional ignitions and agricultural fires.

687 The regional model skill of fire activity was also demonstrated in the simulated
688 burned area. Burned area in southern hemisphere Africa was well simulated by the model,
689 while less active fire regions like temperate and boreal North America, Boreal Asia,
690 Europe, and Middle East were biased high compared to GFED4s. Other regions like
691 Australia, northern sub-Saharan Africa in November-December, Central Asia and
692 Southeast Asia in January-March were biased low. Though the seasonality of simulated
693 burned area reflects that of simulated active fires, the bias of burned area compared to
694 GFED4s data is at least double that of active fires. Burned area is a quantity that most fire
695 models struggle with. Wind speed, a driver of burned area, is averaged over a coarse grid
696 cell, with no feedback from fire heat and energy, which can be a contributing factor to the
697 lower simulated burned area values. The prescribed rudimentary PFTs of the model are a
698 simplified version of the real world and thus can be a source of additional uncertainty.
699 Finally, the rate of spread of burned area, a function of the burning vegetation type, that
700 pyrE and other fire models use is on the lower end of field observations. A higher rate of

701 spread could help to both override the scaling factor used for burned area, and to reduce
702 the negative bias compared to GFED4s.

703 Unlike other fire models, fire emissions in pyrE are driven directly by fires
704 instead of burned area. Emissions are based on online active fires calculations and offline
705 emission factors derived as described in Sect. 2.6. In contrast to the fact that simulated
706 active fires are biased high compared to MODIS, globally, fire emissions are biased low
707 compared to GFED4s. Fire emissions are well-simulated over the southern hemisphere
708 with the exception of Australia. Emissions are biased low over the northern hemisphere
709 including northern sub-Saharan, with the exception of NH South America, which is biased
710 high. The bias of active fires compared to MODIS in Australia and in northern sub-
711 Saharan Africa during November-December propagates to emissions. The emission
712 factors, which were calculated offline using MODIS fire count and GFED4s fire
713 emissions and were applied based on the prescribed PFTs of the model, have their own
714 limitations. They are based on a training dataset of seven years, which would introduce
715 biases in regions where fire cycle is longer than seven years. Also, they rely on the
716 modeled PFTs, enhancing the emissions dependency on the prescribed PFT and the lack
717 of peat. Emission factors do not distinguish between intentional and accidental fires, thus
718 they indirectly account for all fire emissions, which reduce existing biases, although the
719 regional distribution of them will not match the locations of intentional fires, unless
720 natural vegetation burning occurs in the vicinity.

721 Less emissions compared to GFED4s means lower column densities and lower
722 AOD when comparing a simulation with interactive fires to one with prescribed fires.
723 However, as these quantities depend on climate feedbacks including processes other than
724 fire, e.g. additional emission sources, precipitation, deposition, transport, and chemistry,
725 the differences between the two simulations dilute. Nonetheless, a comparison with
726 MODIS AOD demonstrates that AOD from a simulation with interactive fire emissions is
727 comparable to AOD from a simulation with prescribed fire emissions.

728 The work presented here highlights that timing matters just as much as magnitude.
729 This is true for fire distribution, emissions, and atmospheric composition. Timing is also
730 the reason why intentional ignition was excluded from pyrE. Intentional ignition, namely
731 land clearing and agricultural fires, depends on region and crop specific planting and

732 harvesting times. To include it would require crop functionality in ModelE, which was
733 not present during the time of our development. Further future development should focus
734 on the inclusion of intentional ignition and agricultural fires which are seasonal in nature,
735 derived from crop planting and land clearing times. This addition could perhaps improve
736 model performance over regions like equatorial Asia, Southeast Asia, and Central
737 America as well as override the global scaling factors applied to active fires and burned
738 area. The use of scaling factors is a common practice among fire models, and should be
739 carefully and transparently documented. Also, enhancing the prescribed PFTs, especially
740 via the addition of peat is imperative when studying fires. Peat exists as well outside of
741 tropical Asia. There are immense reservoirs of peat in Africa [*Dargie et al.*, 2017], as
742 well as the boreal regions [Yu, 2012], where it used to be trapped under permafrost. Peat
743 will likely become an even bigger source of fire emissions in the future. Improvement of
744 the cloud to ground lightning parameterization may also prove useful, as changes to
745 natural ignition will likely have significant impacts on Australian and boreal fire
746 emissions. Finally, given that the heat component of fires interact with the climate system,
747 and can also be used to derive more accurate emissions, as demonstrated by *Ichoku and*
748 *Ellison* (2014) and three of the eleven FireMIP models (*Rabin et al.*, 2017), it is
749 worthwhile taking it into consideration when developing new fire modeling capabilities.

750 **7 Code availability**

751 Information on ModelE, including access to online data and descriptions are available at
752 <http://www.giss.nasa.gov/tools/modelE>. The pyrE module is included in ModelE version
753 2.1. The source code, along with documentation, can be downloaded from the NASA
754 Goddard Institute of Space Studies website: <https://simplex.giss.nasa.gov/snapshots/>.

755 **Acknowledgements.** Climate modeling at GISS is supported by the NASA Modeling,
756 Analysis, and Prediction program. The authors acknowledge funding from NASA's
757 Atmospheric Composition Modeling and Analysis Program (ACMAP), contract
758 NNX15AE36G. Resources supporting this work were provided by the NASA High-End
759 Computing (HEC) Program through the NASA Center for Climate Simulation (NCCS) at
760 Goddard Space Flight Center.

761

762 **References**

- 763 Akagi, S. K., R. J. Yokelson, C. Wiedinmyer, M. J. Alvarado, J. S. Reid, T. Karl, J. D.
764 Crounse, and P. O. Wennberg: Emission factors for open and domestic biomass
765 burning for use in atmospheric models, *Atmos. Chem. Phys.*, *11*(9), 4039–4072,
766 doi:10.5194/acp-11-4039-2011, 2011.
- 767 Andela, N., and G. R. Van Der Werf : Recent trends in African fires driven by cropland
768 expansion and El Niño to La Niña transition, *4*(September), 791–795,
769 doi:10.1038/NCLIMATE2313, 2014.
- 770 Andela, N., D. C. Morton, L. Giglio, Y. Chen, G. R. van der Werf, P. S. Kasibhatla, R. S.
771 DeFries, G. J. Collatz, S. Hantson, S. Kloster, D. Bachelet, M. Forrest, G. Lasslop, F.
772 Li, S. Mangeon, J. R. Melton, C. Yue, J. T. Randerson: A human-driven decline in
773 global burned area, *1362*(June), 1356–1362, 2017.
- 774 Andreae, M. O.: Biomass burning: Its history, use, and distribution and its impact on
775 environmental quality and global climate, in *Global Biomass Burning: Atmospheric,*
776 *Climate and Biospheric implications*, edited by J. S. Levine, *MIT Press. Cambridge,*
777 *Mass.*, 3–21, 1991.
- 778 Andreae, M. O., and P. Merlet: Emission of trace gases and aerosols from biomass
779 burning, *Global Biogeochem. Cycles*, *15*(4), 955–966, doi:10.1029/2000GB001382,
780 2001.
- 781 Andreae, M. O., D. Rosenfeld, P. Artaxo, A. A. Costa, G. P. Frank, K. M. Longo, and M.
782 A. F. Silva-Dias: Smoking rain clouds over the Amazon., *Science*, *303*, 1337–1342,
783 doi:10.1126/science.1092779, 2004.
- 784 Andreae, M. O. (2019), Emission of trace gases and aerosols from biomass burning – an
785 updated assessment, *Atmos. Chem. Phys.*, *19*, 8523–8546,
786 <https://doi.org/10.5194/acp-19-8523-2019>.
- 787 Archibald, S., A. C. Staver, and S. A. Levin: Evolution of human-driven fire regimes in
788 Africa, *Proc. Natl. Acad. Sci.*, *109*(3), 847–852, doi:10.1073/pnas.1118648109,
789 2012.
- 790 Archibald S. 2016: Managing the human component of fire regimes: lessons from Africa.
791 *Phil. Trans. R. Soc. B* 371: 20150346. <http://dx.doi.org/10.1098/rstb.2015.0346>
- 792 Arora, V. K., and G. J. Boer: Fire as an interactive component of dynamic vegetation

793 models, *J. Geophys. Res.*, *110*, doi:10.1029/2005JG000042, 2005.

794 Balch, J. K., B. A. Bradley, J. T. Abatzoglou, R. C. Nagy, and E. J. Fusco: Human-started
795 wildfires expand the fire niche across the United States, , *114*(11),
796 doi:10.1073/pnas.1617394114, 2017.

797 Bachelet, D., Ferschweiler, K., Sheehan, T. J., Sleeter, B. M., and Zhu, Z.: Projected
798 carbon stocks in the conterminous USA with land use and variable fire regimes,
799 *Glob. Change Biol.*, *21*, 4548– 4560, doi:10.1111/gcb.13048, 2015.

800 Bauer, S.E., D. Wright, D. Koch, E.R. Lewis, R. McGraw, L.-S. Chang, S.E. Schwartz,
801 and R. Ruedy: MATRIX (Multiconfiguration Aerosol TRacker of mIXing state): An
802 aerosol microphysical module for global atmospheric models. *Atmos. Chem. Phys.*,
803 *8*, 6603-6035, doi:10.5194/acp-8-6003-2008, 2008.

804 Bauer, S. E., and S. Menon: Aerosol direct , indirect , semidirect , and surface albedo
805 effects from sector contributions based on the IPCC AR5 emissions for preindustrial
806 and present-day conditions, , *117*, 1–15, doi:10.1029/2011JD016816, 2012.

807 Bauer, S. E., U. Im, K. Mezuman, and C. Y. Gao: Desert dust, industrialization and
808 agricultural fires: Health impacts of outdoor air pollution in Africa, *J. Geophys. Res.*
809 *Atmos.*, 1–17, doi:10.1029/2018JD029336, 2019.

810 Bellouin, N., A. Jones, J. Haywood, and S. A. Christopher: Updated estimate of aerosol
811 direct Radiative forcing from satellite observations and comparison against the
812 centre climate model, *J. Geophys. Res. Atmos.*, *113*(10), 1–15,
813 doi:10.1029/2007JD009385, 2008.

814 Bond, T. C., and R. W. Bergstrom: Light Absorption by Carbonaceous Particles: An
815 Investigative Review, *Aerosol Sci. Technol.*, *40*(1), 27–67,
816 doi:10.1080/02786820500421521, 2006.

817 Bowman, D. M. J. S., J. K. Balch, P. Artaxo, W. J. Bond, J. M. Carlson, M. A. Cochrane,
818 C. M. D’Antonio, R. S. DeFries, J. C. Doyle, S. P. Harrison, F. H. Johnston, J. E.
819 Keeley, M. A. Krawchuk, C. A. Kull, J. B. Marston, M. A. Moritz, I. C. Prentice, C.
820 I. Roos, A. C. Scott, T. W. Swetnam, G. R. van der Werf, and S. J. Pyne: Fire in the
821 Earth System, *Science*, *324*(5926), 481–484, doi:10.1126/science.1163886, 2009.

822 Bowman, D. M. J. S., J. Balch, P. Artaxo, W. J. Bond, M. A. Cochrane, C. M. D’Antonio,
823 R. DeFries, F. H. Johnston, J. E. Keeley, M. A. Krawchuk, C. A. Kull, M. Mack, M.

824 A. Moritz, S. Pyne, C. I. Roos, A. C. Scott, N. S. Sodhi, and T. W. Swetnam: The
825 human dimension of fire regimes on Earth, *J. Biogeogr.*, 38(12), 2223–2236,
826 doi:10.1111/j.1365-2699.2011.02595.x, 2011.

827 Buchholz, R. R., D. Hammerling, H. M. Worden, M. N. Deeter, L. K. Emmons, D. P.
828 Edwards, and S. A. Monks: Links Between Carbon Monoxide and Climate Indices
829 for the Southern Hemisphere and Tropical Fire Regions, *J. Geophys. Res. Atmos.*,
830 123(17), 9786–9800, doi:10.1029/2018JD028438, 2018.

831 Butsic, V., M. Kelly, and M. Moritz: Land Use and Wildfire: A Review of Local
832 Interactions and Teleconnections, *Land*, 4(1), 140–156, doi:10.3390/land4010140,
833 2015.

834 Carslaw, K. S., L. A. Lee, C. L. Reddington, K. J. Pringle, A. Rap, P. M. Forster, G. W.
835 Mann, D. V. Spracklen, M. T. Woodhouse¹, L. A. Regayre, and J. R. Pierce: Large
836 contribution of natural aerosols to uncertainty in indirect forcing., *Nature*, 503(7474),
837 67–71, doi:10.1038/nature12674, 2013.

838 Chuvieco, E., C. Yue, A. Heil, F. Mouillot, I. Alonso-canas, M. Padilla, J. M. Pereira, D.
839 Oom, and K. Tansey: METHODS A new global burned area product for climate
840 assessment of fire impacts, , 45, 619–629, doi:10.1111/geb.12440, 2016.

841 Crutzen, P. J., L. E. Heidt, J. P. Krasnec, W. H. Pollock, and W. Seiler: Biomass burning
842 as a source of atmospheric gases CO, H₂, N₂O, NO, CH₃Cl and COS, *Nature*, 282,
843 253–256, doi:10.1038/282253a0.

844 Crutzen, P. J., and M. O. Andreae (1990), Biomass burning in the tropics: impact on
845 atmospheric chemistry and biogeochemical cycles., *Science*, 250, 1669–1678,
846 doi:10.1126/science.250.4988.1669, 1979.

847 Díaz-Avalos, C., D. L. Peterson, E. Alvarado, S. a Ferguson, and J. E. Besag: Space–time
848 modelling of lightning-caused ignitions in the Blue Mountains, Oregon, *Can. J. For.*
849 *Res.*, 31, 1579–1593, doi:10.1139/cjfr-31-9-1579, 2001.

850 Dwyer, E., S. Pinnock, J. M. Gregoire, and J. M. C. Pereira: Global spatial and temporal
851 distribution of vegetation fire as determined from satellite observations, *Int. J.*
852 *Remote Sens.*, 21(6–7), 1289–1302, doi:10.1080/014311600210182, 2000.

853 Feingold, G., L. A. Remer, J. Ramaprasad, and Y. J. Kaufman: Analysis of smoke impact
854 on clouds in Brazilian biomass burning regions: An extension of Twomey’s

855 approach, *J. Geophys. Res.*, *106*(D19), 22907, doi:10.1029/2001JD000732, 2001.

856 Field, R. D., G. R. van der Werf, T. Faninc, E. J. Fetzerd, R. Fullerd, H. Jethvae, R.
857 Levye, N. J. Liveseyd, M. Luod, O. Torrese, and H. M. Worden: Indonesian fire
858 activity and smoke pollution in 2015 show persistent nonlinear sensitivity to El
859 Niño-induced drought, *Proc. Natl. Acad. Sci.*, *113*(33), 9204–9209,
860 doi:10.1073/pnas.1524888113, 2016.

861 Fischer, A. P., T. A. Spies, T. A. Steelman, C. Moseley, B. R. Johnson, J. D. Bailey,
862 A. A. Ager, P. Bourgeron, S. Charnley, B. M. Collins, J. D. Kline, J. E. Leahy,
863 J. S. Littell, J. D. A. Millington, M. Nielsen-Pincus, C. S. Olsen, T. B. Paveglio, C. I.
864 Roos, M. M. Steen-Adams, F. R. Stevens, J. Vukomanovic, E. M. White, and D. M.
865 J. S. Bowman: Wildfire risk as a socioecological pathology, *Front. Ecol. Environ.*,
866 *14*(5), 276–284, doi:10.1002/fee.1283, 2016.

867 Forkel, M., W. Dorigo, G. Lasslop, I. Teubner, E. Chuvieco, and K. Thonicke: A data-
868 driven approach to identify controls on global fire activity from satellite and climate
869 observations (SOFIA V1), *Geosci. Model Dev.*, *10*(12), 4443–4476,
870 doi:10.5194/gmd-10-4443-2017, 2017.

871 Forkel, M., N. Andela, S. P. Harrison, G. Lasslop, M. van Marle, E. Chuvieco, W. Dorigo,
872 M. Forrest, S. Hantson, A. Heil, F. Li, J. Melton, S. Sitch, C. Yue, and A. Arneith:
873 Emergent relationships with respect to burned area in global satellite observations
874 and fire-enabled vegetation models, *Biogeosciences*, *16*(1), 57–76, doi:10.5194/bg-
875 16-57-2019, 2019.

876 Friedl, M. A., D. Sulla-Menashe, B. Tan, A. Schneider, N. Ramankutty, A. Sibley, and X.
877 Huang: MODIS Collection 5 global land cover: Algorithm refinements and
878 characterization of new datasets, *Remote Sens. Environ.*, *114*, 168–182,
879 doi:10.1016/j.rse.2009.08.016, 2010.

880 Ganteaume, A., A. Camia, M. Jappiot, J. San-Miguel-Ayanz, M. Long-Fournel, and C.
881 Lampin: A review of the main driving factors of forest fire ignition over Europe,
882 *Environ. Manage.*, *51*(3), 651–662, doi:10.1007/s00267-012-9961-z, 2013.

883 Giglio, L.: MODIS Collection 5 Active Fire Product User’s Guide Version 2.5, *Sci. Syst.*
884 *Appl. Inc.*, (March), 61, 2013.

885 Giglio, L., J. D. Kendall, and R. Mack: A multi-year active fire dataset for the tropics

886 derived from the TRMM VIRS, *Int. J. Remote Sens.*, 24(22), 4505–4525,
887 doi:10.1080/0143116031000070283, 2003a.

888 Giglio, L., J. Desloîtres, C. O. Justice, and Y. J. Kaufman: An enhanced contextual fire
889 detection algorithm for MODIS, *Remote Sens. Environ.*, 87(2–3), 273–282,
890 doi:10.1016/S0034-4257(03)00184-6, 2003b.

891 Giglio, L., I. Csiszar, and C. O. Justice: Global distribution and seasonality of active fires
892 as observed with the Terra and Aqua Moderate Resolution Imaging
893 Spectroradiometer (MODIS) sensors, *J. Geophys. Res. Biogeosciences*, 111(2), 1–12,
894 doi:10.1029/2005JG000142, 2006.

895 Giglio, L., J. T. Randerson, and G. R. Van Der Werf: Analysis of daily, monthly, and
896 annual burned area using the fourth-generation global fire emissions database
897 (GFED4), *J. Geophys. Res. Biogeosciences*, 118(1), 317–328,
898 doi:10.1002/jgrg.20042, 2013.

899 Goff, J. A.: Saturation pressure of water on the new Kelvin temperature scale, in
900 *Transactions of the American Society of Heating and Ventilating Engineers, 63rd*
901 *Semi-Annual Meeting*, pp. 347–354, Am. Soc. of Heating and Ventilating Eng.,
902 Murray Bay, Quebec, Canada, 1957.

903 Goff, J. A., and S. Gratch: Low-pressure properties of water from 160 to 212F, in
904 *Transactions of the American Society of Heating and Ventilating Engineers, 52nd*
905 *Annual Meeting*, pp. 95–122, Am. Soc. of Heating and Ventilating Eng., New York,
906 1946.

907 Hamilton, D. S., S. Hantson, C. E. Scott, J. O. Kaplan, K. J. Pringle, L. P. Nieradzik, A.
908 Rap, G. A. Folberth, D. V. Spracklen, and K. S. Carslaw: Reassessment of pre-
909 industrial fire emissions strongly affects anthropogenic aerosol forcing, *Nat.*
910 *Commun.*, 9(1), doi:10.1038/s41467-018-05592-9, 2018.

911 Hantson, S., G. Lasslop, S. Kloster, and E. Chuvieco: Anthropogenic effects on global
912 mean fire size, *Int. J. Wildl. Fire*, 24(5), 589–596, doi:10.1071/WF14208, 2015.

913 Hantson, S., A. Arneth, S. P. Harrison, D. I. Kelley, I. C. Prentice, S. S. Rabin, S.
914 Archibald, F. Mouillot, S. R. Arnold, P. Artaxo, D. Bachelet, P. Ciais, M. Forrest, P.
915 Friedlingstein, T. Hickler, J. O. Kaplan, S. Kloster, W. Knorr, G. Lasslop, F. Li, S.
916 Mangeon, J. R. Melton, A. Meyn, S. Sitch, A. Spessa, G. R. van der Werf, A.

917 Voulgarakis, and C. Yue: The status and challenge of global fire modelling,
918 *Biogeosciences*, 13(11), 3359–3375, doi:10.5194/bg-13-3359-2016, 2016.

919 Hantson, S., M. Scheffer, S. Pueyo, C. Xu, G. Lasslop, E. H. Van Nes, M. Holmgren, and
920 J. Mendelsohn: Rare, Intense, Big fires dominate the global tropics under drier
921 conditions, *Sci. Rep.*, 7(1), 7–11, doi:10.1038/s41598-017-14654-9, 2017.

922 Hoesly, R. M., S. J. Smith, L. Feng, Z. Klimont, G. Janssens-Maenhout, T. Pitkanen, J. J.
923 Seibert, L. Vu, R. J. Andres, R. M. Bolt, T. C. Bond, L. Dawidowski, N. Kholod, J.
924 Kurokawa, M. Li, L. Liu, Z. Lu, M. C. P. Moura, P. R. O'Rourke, and Q. Zhang:
925 Historical (1750–2014) anthropogenic emissions of reactive gases and aerosols from
926 the Community Emissions Data System (CEDS), *Geosci. Model Dev.*, 11(1), 369–
927 408, doi:10.5194/gmd-11-369-2018, 2018.

928 Ichoku, C., L. Giglio, M. J. Wooster, and L. A. Remer: Global characterization of
929 biomass-burning patterns using satellite measurements of fire radiative energy,
930 *Remote Sens. Environ.*, 112(6), 2950–2962, doi:10.1016/j.rse.2008.02.009, 2008.

931 Ichoku, C., and L. Ellison: Global top-down smoke-aerosol emissions estimation using
932 satellite fire radiative power measurements, *Atmos. Chem. Phys.*, 14, 6643–6667,
933 doi:10.5194/acp-14-6643-2014, 2014.

934 Ichoku, C., R. Kahn, and M. Chin: Satellite contributions to the quantitative
935 characterization of biomass burning for climate modeling, *Atmos. Res.*, 111, 1–28,
936 doi:10.1016/j.atmosres.2012.03.007, 2012.

937 Ito, A., and J. E. Penner: Historical emissions of carbonaceous aerosols from biomass and
938 fossil fuel burning for the period 1870-2000, *Global Biogeochem. Cycles*, 19(2), 1–
939 14, doi:10.1029/2004GB002374, 2005.

940 Jiang, Y., Z. Lu, X. Liu, Y. Qian, K. Zhang, Y. Wang, and X.-Q. Yang: Impacts of
941 Global Wildfire Aerosols on Direct Radiative, Cloud and Surface-Albedo Forcings
942 Simulated with CAM5, *Atmos. Chem. Phys.*, 16, 14805–14824, doi:10.5194/acp-16-
943 14805-2016, 2016.

944 Johnson, B. T., J. M. Haywood, J. M. Langridge, E. Darbyshire, W. T. Morgan, K. Szpek,
945 J. K. Brooke, F. Marenco, H. Coe, P. Artaxo, K. M. Longo, J. P. Mulcahy, G. W.
946 Mann, M. Dalvi, and N. Bellouin: Evaluation of biomass burning aerosols in the
947 HadGEM3 climate model with observations from the SAMBBA field campaign, ,

948 14657–14685, doi:10.5194/acp-16-14657-2016, 2016.

949 Johnston, F. H., S. B. Henderson, Y. Chen, J. T. Randerson, M. Marlier, R. S. Defries, P.
950 Kinney, D. M. J. S. Bowman, and M. Brauer: Estimated Global Mortality
951 Attributable to Smoke from Landscape Fires, , *J20(5)*, 695–701, 2012.

952 Johnston, F. H., S. Purdie, B. Jalaludin, K. L. Martin, S. B. Henderson, and G. G. Morgan:
953 Air pollution events from forest fires and emergency department attendances in
954 Sydney, Australia 1996-2007: A case-crossover analysis, *Environ. Heal. A Glob.*
955 *Access Sci. Source*, *13(1)*, 1–9, doi:10.1186/1476-069X-13-105, 2014.

956 Johnston, F. H., S. Melody, and D. M. J. S. Bowman: The pyrohealth transition: How
957 combustion emissions have shaped health through human history, *Philos. Trans. R.*
958 *Soc. B Biol. Sci.*, *371(1696)*, doi:10.1098/rstb.2015.0173, 2016.

959 Justice, C. ., L. Giglio, S. Korontzi, J. Owens, J. . Morisette, D. Roy, J. Descloitres, S.
960 Alleaume, F. Petitcolin, and Y. Kaufman: The MODIS fire products, *Remote Sens.*
961 *Environ.*, *83(1–2)*, 244–262, doi:10.1016/S0034-4257(02)00076-7, 2002.

962 Kaiser, J. W., A. Heil, M. O. Andreae, A. Benedetti, N. Chubarova, L. Jones, J.-J.
963 Morcrette, M. Razinger, M. G. Schultz, M. Suttie, and G. R. van der Werf: Biomass
964 burning emissions estimated with a global fire assimilation system based on
965 observed fire radiative power, *Biogeosciences*, *9(1)*, 527–554, doi:10.5194/bg-9-
966 527-2012, 2012.

967 Kaufman, Y. J., A. E. Wald, L. A. Remer, B. C. Gao, R. R. Li, and L. Flynn: MODIS
968 2.1- μm channel - correlation with visible reflectance for use in remote sensing of
969 aerosol, *IEEE Trans. Geosci. Remote Sens.*, *35(5)*, 1286–1298,
970 doi:10.1109/36.628795, 1997.

971 Keetch, J. J. J. J., and G. M. G. M. Byram: A drought index for forest fire control, *Notes*,
972 *E-38. Ashe*, *35*, doi:10.1016/j.accpm.2015.04.007, 1968.

973 Kim, Y., P. R. Moorcroft, I. Aleinov, M. J. Puma, and N. Y. Kiang: Variability of
974 phenology and fluxes of water and carbon with observed and simulated soil moisture
975 in the Ent Terrestrial Biosphere Model (Ent TBM version 1.0.1.0.0), *Geosci. Model*
976 *Dev.*, *8(12)*, 3837–3865, doi:10.5194/gmd-8-3837-2015, 2015.

977 Klein Goldewijk, K., a. Beusen, and P. Janssen: Long-term dynamic modeling of global
978 population and built-up area in a spatially explicit way: HYDE 3.1, *The Holocene*,

979 20(4), 565–573, doi:10.1177/0959683609356587, 2010.

980 Lack, D. A., J. M. Langridge, R. Bahreini, C. D. Cappa, and A. M. Middlebrook: Brown
981 carbon and internal mixing in biomass burning particles, , *109*(37),
982 doi:10.1073/pnas.1206575109/-
983 /DCSupplemental.www.pnas.org/cgi/doi/10.1073/pnas.1206575109, 2012.

984 Lack, D. a., and J. M. Langridge: On the attribution of black and brown carbon light
985 absorption using the Ångström exponent, *Atmos. Chem. Phys.*, *13*(20), 10535–10543,
986 doi:10.5194/acp-13-10535-2013, 2013.

987 Lamarque, J. F., T. C. Bond, V. Eyring, C. Granier, A. Heil, Z. Klimont, D. Lee, C.
988 Lioussé, A. Mieville, B. Owen, M. G. Schultz, D. Shindell, S. J. Smith, E. Stehfest, J.
989 Van Aardenne, O. R. Cooper, M. Kainuma, N. Mahowald, J. R. McConnell, V. Naik,
990 K. Riahi, and D. P. van Vuuren: Historical (1850–2000) gridded anthropogenic and
991 biomass burning emissions of reactive gases and aerosols: methodology and
992 application, *Atmos. Chem. Phys.*, *10*(15), 7017–7039, doi:10.5194/acp-10-7017-
993 2010, 2010.

994 Landry, J.-S., and H. D. Matthews: Non-deforestation fire vs. fossil fuel combustion: the
995 source of CO₂ emissions affects the global carbon cycle and climate responses,
996 *Biogeosciences*, *13*(7), 2137–2149, doi:10.5194/bg-13-2137-2016, 2016.

997 Laskin, A., J. Laskin, and S. A. Nizkorodov: Chemistry of Atmospheric Brown Carbon,
998 *Chem. Rev.*, *115*(10), 4335–4382, doi:10.1021/cr5006167, 2015.

999 Lasslop, G., K. Thonicke, and S. Kloster: SPITFIRE within the MPI Earth system model:
1000 Model development and evaluation, *J. Adv. Model. Earth Syst.*, *6*, 740–755,
1001 doi:10.1002/2013MS000284.Received, 2014.

1002 Lasslop, G., A. I. Coppola, A. Voulgarakis, C. Yue, and S. Veraverbeke: Influence of
1003 Fire on the Carbon Cycle and Climate, *Curr. Clim. Chang. Reports*,
1004 doi:10.1007/s40641-019-00128-9, 2019.

1005 Lelieveld, J., J. S. Evans, M. Fnais, D. Giannadaki, and A. Pozzer: The contribution of
1006 outdoor air pollution sources to premature mortality on a global scale., *Nature*,
1007 *525*(7569), 367–71, doi:10.1038/nature15371, 2015.

1008 Levy, R. C., S. Mattoo, L. A. Munchak, L. A. Remer, A. M. Sayer, F. Patadia, and N. C.
1009 Hsu: The Collection 6 MODIS aerosol products over land and ocean, *Atmos. Meas.*

1010 *Tech.*, 6(11), 2989–3034, doi:10.5194/amt-6-2989-2013, 2013.

1011 Li, F., X. D. Zeng, and S. Levis: A process-based fire parameterization of intermediate
1012 complexity in a dynamic global vegetation model, *Biogeosciences*, 9(7), 2761–2780,
1013 doi:10.5194/bg-9-2761-2012, 2012.

1014 Lindeskog, M., Arneth, A., Bondeau, A., Waha, K., Seaquist, J., Olin, S., and Smith, B.:
1015 Implications of accounting for land use in simulations of ecosystem carbon cycling
1016 in Africa, *Earth Syst. Dynam.*, 4, 385–407, doi:10.5194/esd-4-385-2013, 2013.

1017 Mangeon, S., A. Voulgarakis, R. Gilham, A. Harper, S. Sitch, and G. Folberth:
1018 INFERNO : a fire and emissions scheme for the UK Met Office’s Unified Model,
1019 2685–2700, doi:10.5194/gmd-9-2685-2016, 2016.

1020 Mao, J., L. W. Horowitz, V. Naik, S. Fan, J. Liu, and A. M. Fiore: Sensitivity of
1021 tropospheric oxidants to biomass burning emissions: Implications for radiative
1022 forcing, *Geophys. Res. Lett.*, 40(2), 1241–1246, doi:10.1002/grl.50210, 2013.

1023 Marlon , J. R., P. J. Bartlein, D G. Gavin, C. J. Long, R. S. Anderson, C. E. Briles, K. J.
1024 Brown, D. Colombaroli, D. J. Hallett, M. J. Power, E. A. Scharf, M. K. Walsh:
1025 Long-term perspective on wildfires in the western USA. *Proceedings of the National*
1026 *Academy of Sciences*, 109 (9) E535-E543; DOI: 10.1073/pnas.1112839109, 2012.

1027 Van Marle, M.J.E., S. Kloster, B.I. Magi, J.R. Marlon, A.-L. Daniau, R.D. Field, A.
1028 Arneth, M. Forrest, S. Hantson, N.M. Kehrwald, W. Knorr, G. Lasslop, F. Li, S.
1029 Mangeon, C. Yue, J.W. Kaiser, and G.R. van der Werf: Historic global biomass
1030 burning emissions for CMIP6 (BB4CMIP) based on merging satellite observations
1031 with proxies and fire models (1750-2015). *Geosci. Model Dev.*, 10, 3329-3357,
1032 doi:10.5194/gmd-10-3329-2017, 2017.

1033 Moritz, M. A., E. Batllori, R. A. Bradstock, A. M. Gill, J. Handmer, P. F. Hessburg, J.
1034 Leonard, S. McCaffrey, D. C. Odion, T. Schoennagel, and A. D. Syphard: Learning
1035 to coexist with wildfire, *Nature*, 515(7525), 58–66, doi:10.1038/nature13946, 2014.

1036 Murray, L. T.: Lightning NO_x and Impacts on Air Quality, *Curr. Pollut. Reports*, (x),
1037 doi:10.1007/s40726-016-0031-7, 2016.

1038 Pan, X., Ichoku, C., Chin, M., Bian, H., Darmenov, A., Colarco, P., Ellison, L., Kucsera,
1039 T., da Silva, A., Wang, J., Oda, T., and Cui, G. (2020): Six Global Biomass Burning
1040 Emission Datasets: Inter-comparison and Application in one Global Aerosol Model,

1041 *Atmos. Chem. Phys.*, 20, 969-994, <https://doi.org/10.5194/acp-20-969-2020>.
1042 M.-A. Parisien, M.A. Moritz: Environmental controls on the distribution of wildfire at
1043 multiple spatial scales
1044 *Ecol. Monogr.*, 79 (2009), pp. 127-154, 10.1890/07-1289.1
1045 Pechony, O., and D. T. Shindell: Fire parameterization on a global scale, *J. Geophys. Res.*
1046 *Atmos.*, 114, doi:10.1029/2009JD011927, 2009.
1047 Pechony, O., and D. T. Shindell: Driving forces of global wildfires over the past
1048 millennium and the forthcoming century, *Proc. Natl. Acad. Sci.*, 107(45), 19167–
1049 19170, doi:10.1073/pnas.1003669107, 2010.
1050 Pechony, O., D. T. Shindell, and G. Faluvegi: Direct top-down estimates of biomass
1051 burning CO emissions using TES and MOPITT versus bottom-up GFED inventory,
1052 *J. Geophys. Res. Atmos.*, 118, 8054–8066, doi:10.1002/jgrd.50624, 2013.
1053 Pfeifer, E. M., a. Spessa, and J. O. Kaplan: A model for global biomass burning in
1054 preindustrial time: LPJ-LMfire (v1.0), *Geosci. Model Dev.*, 6, 643–685,
1055 doi:10.5194/gmd-6-643-2013, 2013.
1056 Platnick, S., M. D. King, K. G. Meyer, G. Wind, N. Amarasinghe, B. Marchant, G. T.
1057 Aronold, Z. ZHANG, P. A. Hubanks, B. Ridgway, J. Riedi: MODIS Cloud Optical
1058 Properties: User Guide for the Collection 6/6.1 Level-2 MOD06/MYD06 Product
1059 and Associated Level-3 Datasets,
1060 doi:https://doi.org/10.5067/MODIS/MOD08_M3.006, 2015.
1061 Pongratz, J., C. Reick, T. Raddatz, and M. Claussen: A reconstruction of global
1062 agricultural areas and land cover for the last millennium, *Global Biogeochem.*
1063 *Cycles*, 22, doi:10.1029/2007GB003153, 2008.
1064 Price, C., and D. Rind: A Simple Lightning Parameterization for Calculating Global
1065 Lightning Distributions, *J. Geophys. Res.*, 97(D9), 9919–9933, 1992.
1066 Price, C., and D. Rind: What Determines The Cloud-to-Ground Lightning Fraction,
1067 *Geophys. Res. Lett.*, 20(6), 463–466, 1993.
1068 Rabin, S. S., J. R. Melton, G. Lasslop, D. Bachelet, M. Forrest, and S. Hantson: The Fire
1069 Modeling Intercomparison Project (FireMIP), phase 1 : experimental and analytical
1070 protocols with detailed model descriptions, , 1175–1197, doi:10.5194/gmd-10-1175-
1071 2017, 2017.

1072 Radeloff, V. C., David P. H., H. A. Kramera, M. H. Mockrinb, P. M. Alexandria, A. Bar-
1073 Massadac, V. Butsicd, T. J. Hawbakere, S. Martinuzzia, A. D. Syphardf, and S. I.
1074 Stewart: Rapid growth of the US wildland-urban interface raises wildfire risk, *Proc.*
1075 *Natl. Acad. Sci.*, 201718850, doi:10.1073/pnas.1718850115, 2018.

1076 Randerson, J. T., M. V. Thompson, C. M. Malmstrom, C. B. Field, and I. Y. Fung:
1077 Substrate limitations for heterotrophs: Implications for models that estimate the
1078 seasonal cycle of atmospheric CO₂, *Global Biogeochem. Cycles*, 10(4), 585–602,
1079 doi:10.1029/96GB01981, 1996.

1080 Randerson, J. T., Y. Chen, G. R. Van Der Werf, B. M. Rogers, and D. C. Morton: Global
1081 burned area and biomass burning emissions from small fires, *J. Geophys. Res.*
1082 *Biogeosciences*, 117(4), doi:10.1029/2012JG002128, 2012.

1083 Rayner, N. A., D. E. Parker, E. B. Horton, C. K. Folland, L. V. Alexander, D. P. Rowell,
1084 E. C. Kent, and A. Kaplan: Global analyses of sea surface temperature, sea ice, and
1085 night marine air temperature since the late nineteenth century, *J. Geophys. Res.*,
1086 108(D14), 4407, doi:10.1029/2002JD002670, 2003.

1087 Remer, L. A., Y. J. Kaufman, D. Tanré, S. Mattoo, D. A. Chu, J. V. Martins,
1088 R.-R. Li, C. Ichoku, R. C. Levy, R. G. Kleidman, T. F. Eck, E. Vermote, and B. N.
1089 Holben: The MODIS Aerosol Algorithm, Products, and Validation, *J. Atmos. Sci.*,
1090 62(4), 947–973, doi:10.1175/JAS3385.1, 2005.

1091 Ryan, K. C., E. E. Knapp, and J. M. Varner: Prescribed fire in North American forests
1092 and woodlands: History, current practice, and challenges, *Front. Ecol. Environ.*,
1093 11(SUPPL. 1), doi:10.1890/120329, 2013.

1094 Schmidt, G.A., M. Kelley, L. Nazarenko, R. Ruedy, G.L. Russell, I. Aleinov, M. Bauer,
1095 S.E. Bauer, M.K. Bhat, R. Bleck, V. Canuto, Y.-H. Chen, Y. Cheng, T.L. Clune, A.
1096 Del Genio, R. de Fainchtein, G. Faluvegi, J.E. Hansen, R.J. Healy, N.Y. Kiang, D.
1097 Koch, A.A. Lacis, A.N. LeGrande, J. Lerner, K.K. Lo, E.E. Matthews, S. Menon,
1098 R.L. Miller, V. Oinas, A.O. Oloso, J.P. Perlwitz, M.J. Puma, W.M. Putman, D. Rind,
1099 A. Romanou, M. Sato, D.T. Shindell, S. Sun, R.A. Syed, N. Tausnev, K. Tsigaridis,
1100 N. Unger, A. Voulgarakis, M.-S. Yao, and J. Zhang: Configuration and assessment
1101 of the GISS ModelE2 contributions to the CMIP5 archive. *J. Adv. Model. Earth*
1102 *Syst.*, 6, no. 1, 141-184, doi:10.1002/2013MS000265, 2014.

1103 Schoennagel, T., T. T. Veblen, and W. H. Romme: The Interaction of Fire, Fuels, and
1104 Climate across Rocky Mountain Forests, *Bioscience*, 54(JULY), 393–402,
1105 doi:10.1641/0006-3568(2004)054, 2004.

1106 Schultz, M. G., A. Heil, J. J. Hoelzemann, A. Spessa, K. Thonicke, J. G. Goldammer, A.
1107 C. Held, J. M. C. Pereira, and M. van het Bolscher: Global wildland fire emissions
1108 from 1960 to 2000, *Global Biogeochem. Cycles*, 22(2), doi:10.1029/2007GB003031,
1109 2008.

1110 Scott, A. C., and I. J. Glasspool: The diversification of Paleozoic fire systems and
1111 fluctuations in atmospheric oxygen concentration, *Proc. Natl. Acad. Sci.*, 103(29),
1112 10861–10865, doi:10.1073/pnas.0604090103, 2006.

1113 Seager, R., A. Hooks, A. P. Williams, B. Cook, J. Nakamura, and N. Henderson:
1114 Climatology, variability, and trends in the U.S. Vapor pressure deficit, an important
1115 fire-related meteorological quantity, *J. Appl. Meteorol. Climatol.*, 54(6), 1121–1141,
1116 doi:10.1175/JAMC-D-14-0321.1, 2015.

1117 Seiler, W., and P. J. Crutzen: Estimates of gross and net fluxes of carbon between the
1118 biosphere and the atmosphere from biomass burning, *Clim. Change*, 2, 207–247,
1119 doi:10.1007/BF00137988, 1980.

1120 Sheehan, T., Bachelet, D., and Ferschweiler, K.: Projected major fire and vegetation
1121 changes in the Pacific Northwest of the conterminous United States under selected
1122 CMIP5 climate futures, *Ecol. Model.*, 317, 16–29,
1123 doi:10.1016/j.ecolmodel.2015.08.023, 2015.

1124 Simard, M., N. Pinto, J. B. Fisher, and A. Baccini: Mapping forest canopy height globally
1125 with spaceborne lidar, *J. Geophys. Res. Biogeosciences*, 116, 1–12,
1126 doi:10.1029/2011JG001708, 2011.

1127 Smith, B., Prentice, I. C., and Sykes, M. T.: Representation of vegetation dynamics in the
1128 modelling of terrestrial ecosystems: comparing two contrasting approaches within
1129 European climate space, *Global Ecol. Biogeogr.*, 10, 621–637, doi:10.1046/j.1466-
1130 822X.2001.t01-1-00256.x, 2001.

1131 Smith, B., Wårlind, D., Arneth, A., Hickler, T., Leadley, P., Silt-berg, J., and Zaehle, S.:
1132 Implications of incorporating N cycling and N limitations on primary production in
1133 an individual based dynamic vegetation model, *Biogeosciences*, 11, 2027–2054,

1134 doi:10.5194/bg-11-2027-2014, 2014.

1135 Thonicke, K., S. Venevsky, S. Sitch, and W. Cramer: The role of fire disturbance for
1136 global vegetation dynamics: coupling fire into a Dynamic Global Vegetation Model,
1137 *Glob. Ecol. Biogeogr.*, *10*, 661–677, doi:10.1046/j.1466-822X.2001.00175.x, 2001.

1138 Tian, Y., C. E. Woodcock, Y. Wang, J. L. Privette, N. V. Shabanov, L. Zhou, Y. Zhang,
1139 W. Buermann, J. Dong, B. Veikkanen, Tuomas Häme, K. Andersson, M. Ozdogan,
1140 Y. Knyazikhin, R. B. Myneni: Multiscale analysis and validation of the MODIS LAI
1141 product I. Uncertainty assessment, *Remote Sens. Environ.*, *83*, 414–430,
1142 doi:10.1016/S0034-4257(02)00047-0, 2002a.

1143 Tian, Y., C. E. Woodcock, Y. Wang, J. L. Privette, N. V. Shabanov, L. Zhou, Y. Zhang,
1144 W. Buermann, J. Dong, B. Veikkanen, Tuomas Häme, K. Andersson, M. Ozdogan,
1145 Y. Knyazikhin, R. B. Myneni: Multiscale analysis and validation of the MODIS LAI
1146 product II. Sampling strategy, *Remote Sens. Environ.*, *83*, 431–441,
1147 doi:10.1016/S0034-4257(02)00058-5, 2002b.

1148 Tosca, M. G., D. J. Diner, M. J. Garay, and O. V. Kalashnikova: Human-caused fires
1149 limit convection in tropical Africa: First temporal observations and attribution,
1150 *Geophys. Res. Lett.*, *42*(15), 6492–6501, doi:10.1002/2015GL065063, 2015.

1151 Venevsky, S., K. Thonicke, S. Sitch, and W. Cramer: Simulating fire regimes in human-
1152 dominated ecosystems: Iberian Peninsula case study, *Glob. Chang. Biol.*, *8*, 984–998,
1153 doi:10.1046/j.1365-2486.2002.00528.x, 2002.

1154 Voulgarakis, A., and R. D. Field: Fire Influences on Atmospheric Composition, Air
1155 Quality and Climate, *Curr. Pollut. Reports*, *1*(2), 70–81, doi:10.1007/s40726-015-
1156 0007-z, 2015.

1157 van Wagner, C. E.: A simple fire-growth model, *For. Chron.*, *45*(2), 103–104,
1158 doi:10.5558/tfc45104-2, 1969.

1159 Ward, D. S., S. Kloster, N. M. Mahowald, B. M. Rogers, J. T. Randerson, and P. G. Hess:
1160 The changing radiative forcing of fires: global model estimates for past, present and
1161 future, *Atmos. Chem. Phys.*, *12*(22), 10857–10886, doi:10.5194/acp-12-10857-2012,
1162 2012.

1163 Wei, J., Z. Li, Y. Peng, and L. Sun: MODIS Collection 6.1 aerosol optical depth products
1164 over land and ocean: validation and comparison, *Atmos. Environ.*, *201*(October

1165 2018), 428–440, doi:10.1016/j.atmosenv.2018.12.004, 2019.

1166 van der Werf, G. R.: Continental-Scale Partitioning of Fire Emissions During the 1997 to
1167 2001 El Nino/La Nina Period, *Science*, 303(5654), 73–76,
1168 doi:10.1126/science.1090753, 2004.

1169 van der Werf, G. R., J. T. Randerson, L. Giglio, G. J. Collatz, P. S. Kasibhatla, and a. F.
1170 Arellano: Interannual variability of global biomass burning emissions from 1997 to
1171 2004, *Atmos. Chem. Phys.* 6, 3423–3441, <https://doi.org/10.5194/acp-6-3423-2006>,
1172 2006.

1173 van der Werf, G. R., J. T. Randerson, L. Giglio, G. J. Collatz, M. Mu, P. S. Kasibhatla, D.
1174 C. Morton, R. S. DeFries, Y. Jin, and T. T. van Leeuwen: Global fire emissions and
1175 the contribution of deforestation, savanna, forest, agricultural, and peat fires (1997–
1176 2009), *Atmos. Chem. Phys.*, 10(23), 11707–11735, doi:10.5194/acp-10-11707-2010,
1177 2010.

1178 van der Werf, G. R., J. T. Randerson, L. Giglio, T. T. van Leeuwen, Y. Chen, B. M.
1179 Rogers, M. Mu, M. J. E. van Marle, D. C. Morton, G. J. Collatz, R. J. Yokelson, and
1180 P. S. Kasibhatla: Global fire emissions estimates during 1997–2016, *Earth Syst. Sci.*
1181 *Data*, 9(2), 697–720, doi:10.5194/essd-9-697-2017, 2017.

1182 Whitburn, S., M. Van Damme, L. Clarisse, S. Turquety, C. Clerbaux, and P. Coheur:
1183 Doubling of annual ammonia emissions from the peat fires in Indonesia during the
1184 2015 El Niño, , doi:10.1002/2016GL070620.Received, 2016.

1185 Williams, A. P., R. Seager, A. K. Macalady, M. Berkelhammer, M. A. Crimmins, T. W.
1186 Swetnam, A. T. Trugman, N. Buening, D. Noone, N. G. McDowell, N. Hryniw, C.
1187 I. Mora, and T. Rahn: Correlations between components of the water balance and
1188 burned area reveal new insights for predicting forest fire area in the southwest
1189 United States, *Int. J. Wildl. Fire*, 24(1), 14, doi:10.1071/WF14023, 2015.

1190 Wooster, M. J., and Y. H. Zhang: Boreal forest fires burn less intensely in Russia than in
1191 North America, *Geophys. Res. Lett.*, 31(20), 2–4, doi:10.1029/2004GL020805, 2004.

1192 Zou, Y., Y. Wang, Z. Ke, H. Tian, J. Yang, and Y. Liu: Development of a REgion-
1193 Specific Ecosystem Feedback Fire (RESFire) Model in the Community Earth
1194 System Model, *J. Adv. Model. Earth Syst.*, 11(2), 417–445,
1195 doi:10.1029/2018MS001368, 2019.

1196 **Tables**

1197 Table 1 Fire emission factors for the different plant functional types (PFTs) in ModelE2.1.

1198 Factors are in units of kg per fire per PFT in the grid cell. For organic and black carbon

1199 units kg is substituted with kg of carbon.

PFT	CO	NO _x	SO ₂	NH ₃	Alkenes	Paraffin	OC	BC
Cold Broadleaf	113392	1529	555	2101	106	69.8	3437	767
Deciduous Needle leaf	481485	1559	4168	10722	422	373	36753	1844
Drought Broadleaf	230829	4835	1687	2340	214	108	10667	1382
Evergreen Broadleaf	249906	4905	1438	2847	220	102	10941	1434
Evergreen Needle leaf	146622	1197	972	2277	137	89.1	6537	821
Cold Shrub	105936	241	878	2006	104	72.1	6562	357
Arid Shrub	39268	1009	262	378	36.6	18.5	1479	238
C3 Annual Grass	26761	690	147	313	25.1	13.9	728	173
C3 Arctic Grass	251702	1094	2315	5065	489	226	15551	1159
C3 Perennial Grass	41043	908	270	438	38.8	20.7	1504	257
C4 Grass	117577	3152	795	1196	110	57	4339	726

1200

1201

1202

1203

1204

1205

1206

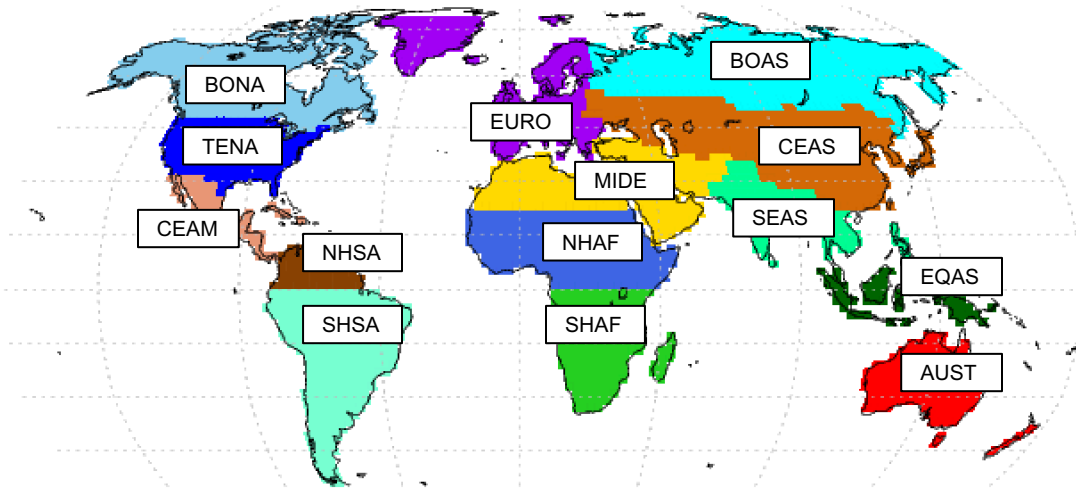
1207

1208 Table 2: Total fire emissions and global mean column loads of fire emitted species.
 1209 Modeled annual emissions and column load means are based on an ensemble of 10
 1210 simulations. GFED4s emissions are based on a 2000-2010 climatological mean.

Species	Variable	pyrE	GFED4s	Bias [%]
CO	Emissions [Tg a ⁻¹]	2.14E+02	3.51E+02	-39
	Column Load [kg m ⁻²]	7.22E-04	7.71E-04	-6.3
OA	Emissions [TgC a ⁻¹]	1.31E+01	2.29E+01	-42
	Column Load [kg m ⁻²]	8.52E-07	1.02E-06	-16
BC	Emissions [TgC a ⁻¹]	1.25E+00	1.84E+00	-32
	Column Load [kg m ⁻²]	7.25E-09	7.62E-09	-4.8
NO _x	Emissions [Tg a ⁻¹]	4.27E+00	6.76E+00	-36
	Column Load [kg m ⁻²]	5.94E-07	5.91E-07	0.5
NH ₃	Emissions [Tg a ⁻¹]	2.43E+00	4.15E+00	-41
	Column Load [kg m ⁻²]	2.15E-07	2.23E-07	-3.5
SO ₂	Emissions [Tg a ⁻¹]	1.34E+00	2.25E+00	-40
	Column Load [kg m ⁻²]	2.67E-06	2.69E-06	-0.7
Alkenes	Emissions [Tg a ⁻¹]	1.94E-01	3.18E-01	-39
	Column Load [kg m ⁻²]	5.73E-08	5.70E-08	0.5
Paraffin	Emissions [Tg a ⁻¹]	9.79E-02	1.65E-01	-40
	Column Load [kg m ⁻²]	2.36E-07	2.42E-07	-2.4

1211
 1212
 1213
 1214
 1215
 1216
 1217
 1218
 1219
 1220

1221 **FIGURES**



1222

- | | |
|----------------------------------------|---------------------------------|
| BONA Boreal North America | NHAF Northern Hemisphere Africa |
| TENA Temperate North America | SHAF Southern Hemisphere Africa |
| CEAM Central America | BOAS Boreal Asia |
| NHSA Northern Hemisphere South America | CEAS Central Asia |
| SHSA Southern Hemisphere South America | SEAS Southeast Asia |
| EURO Europe | EQAS Equatorial Asia |
| MIDE Middle East | AUST Australia and New Zealand |

1223

1224 Figure 1. GFED basis regions regridded to the resolution of ModelE2.1 of 2° in latitude by
1225 2.5° in longitude.

1226

1227

1228

1229

1230

1231

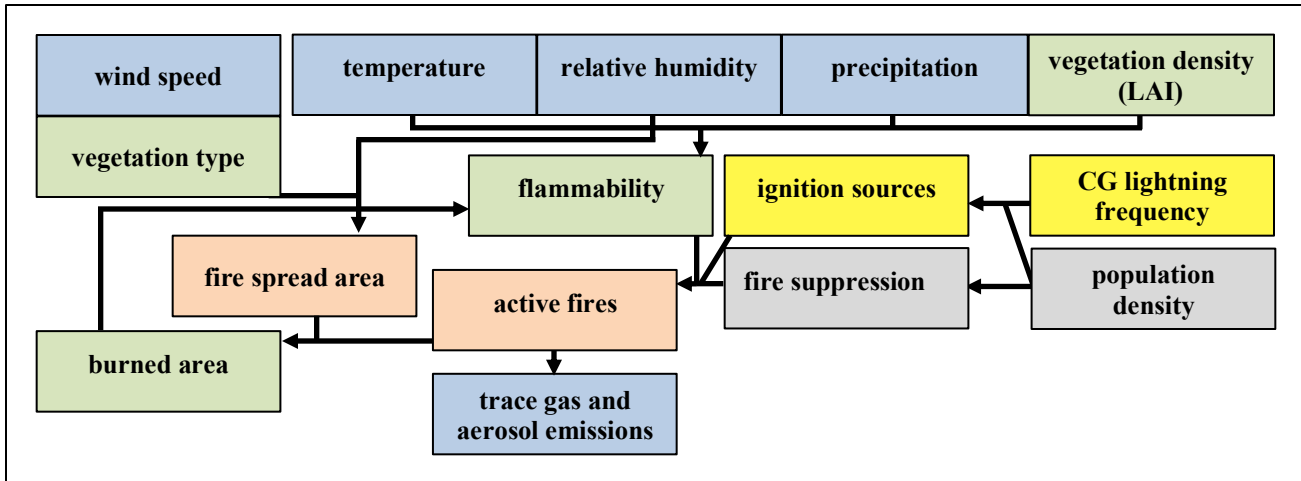
1232

1233

1234

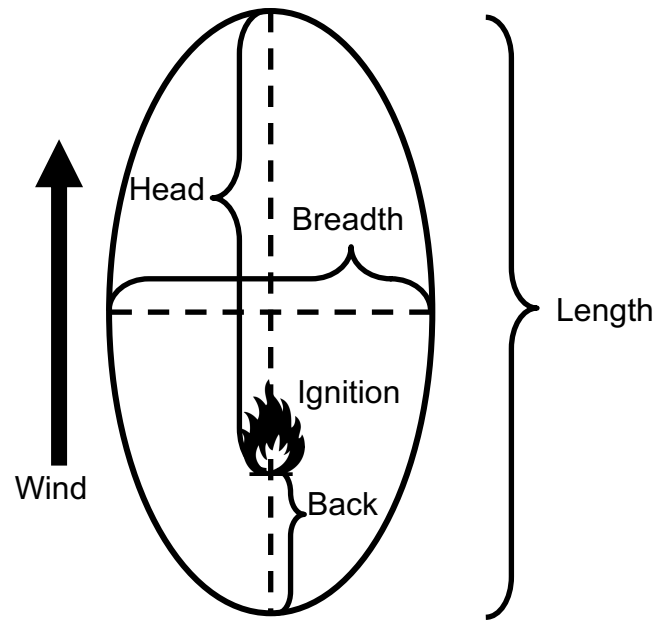
1235

1236



1237 Figure 2. Structure of the fire parameterization of pyrE. Processes related to atmospheric
 1238 properties in blue, surface properties in green, ignition and suppression in yellow and
 1239 gray, and fire properties in red.

1240
 1241
 1242
 1243
 1244
 1245
 1246
 1247
 1248
 1249
 1250
 1251
 1252
 1253
 1254
 1255
 1256
 1257



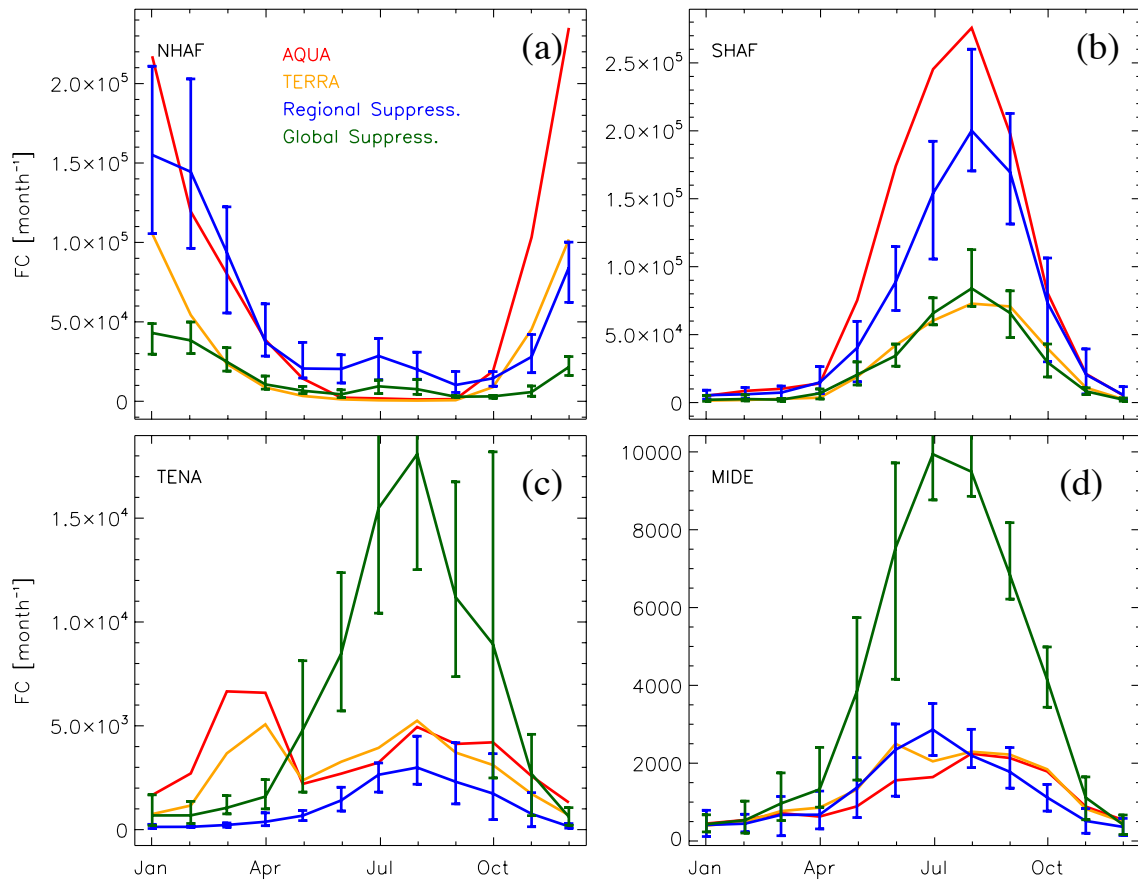
1258

1259

1260 Figure 3. Approximation of a single fire spread. Based on *van Wagner* (1969) and *Arora*

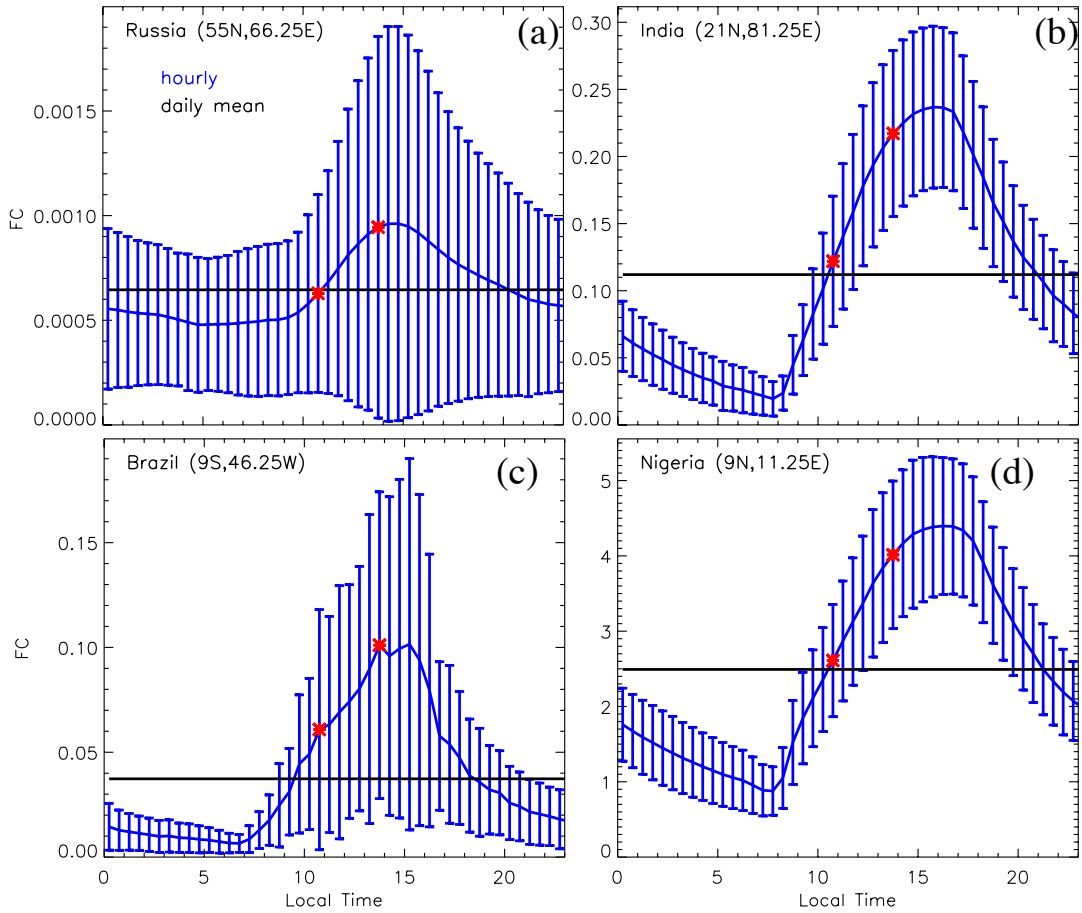
1261 *and Boer* (2005).

1262



1263

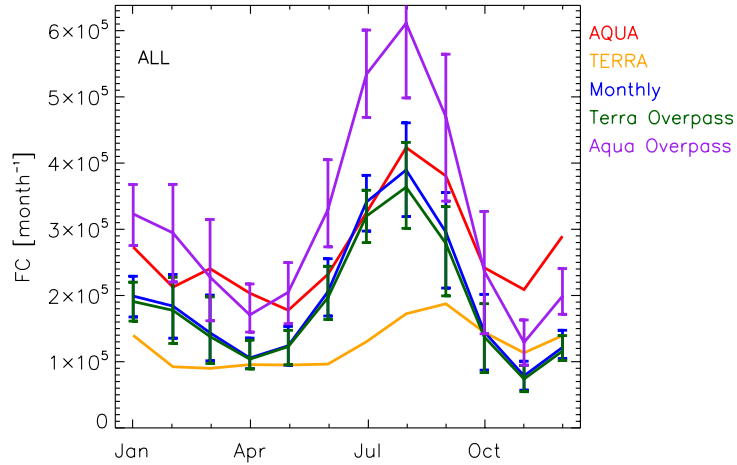
1264 Figure 4: Seasonality of total active fires for NHAF (a), SHAF (b), TENA (c) and
 1265 (d) observed by MODIS Aqua (red) and Terra (orange) and simulated with explicit
 1266 regional suppression (blue) and generic global suppression parameterization (green); Eq.
 1267 6. Error bars represent the range over 10-year climatological simulations. Note that
 1268 TERRA and AQUA have different overpass times, and the model data presented here are
 1269 monthly means. Also, note the different scale in each panel.



1270

1271 Figure 5: Daily mean cycle in active fires (FC, blue line) and daily mean (black line) at 4
 1272 locations (Russia (a), India (b), Brazil (c), Nigeria (d)) during the month of January. The
 1273 daytime overpass times of Terra (10:30am) and Aqua (13:30pm) are marked with a red
 1274 star. Error bars represent the range during the month. Note the different scale in each
 1275 panel.

1276



1277

1278 Figure 6: Global seasonality of total active fires (FC) by MODIS Aqua (red) and Terra
 1279 (orange) and simulated by the model: monthly mean (blue), monthly mean sampled at the
 1280 daytime Terra overpass time (green), and sampled at the daytime Aqua overpass time
 1281 (purple). Error bars represent the 10-year range in the simulation.

1282

1283

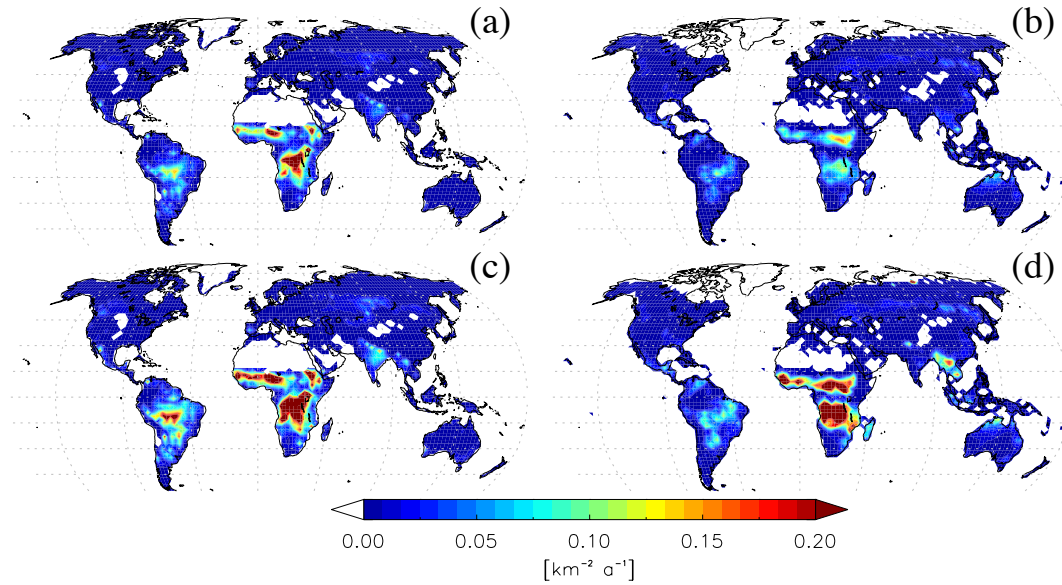
1284

1285

1286

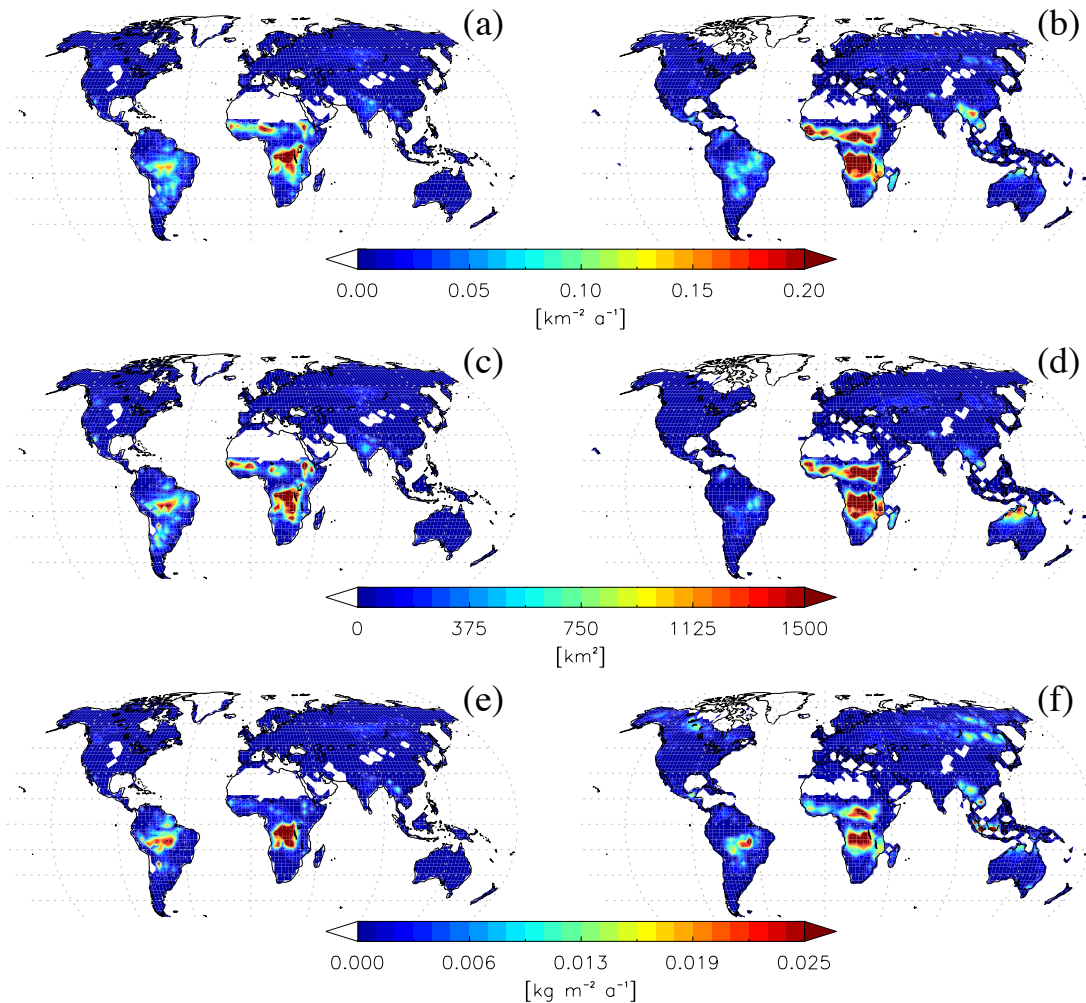
1287

1288



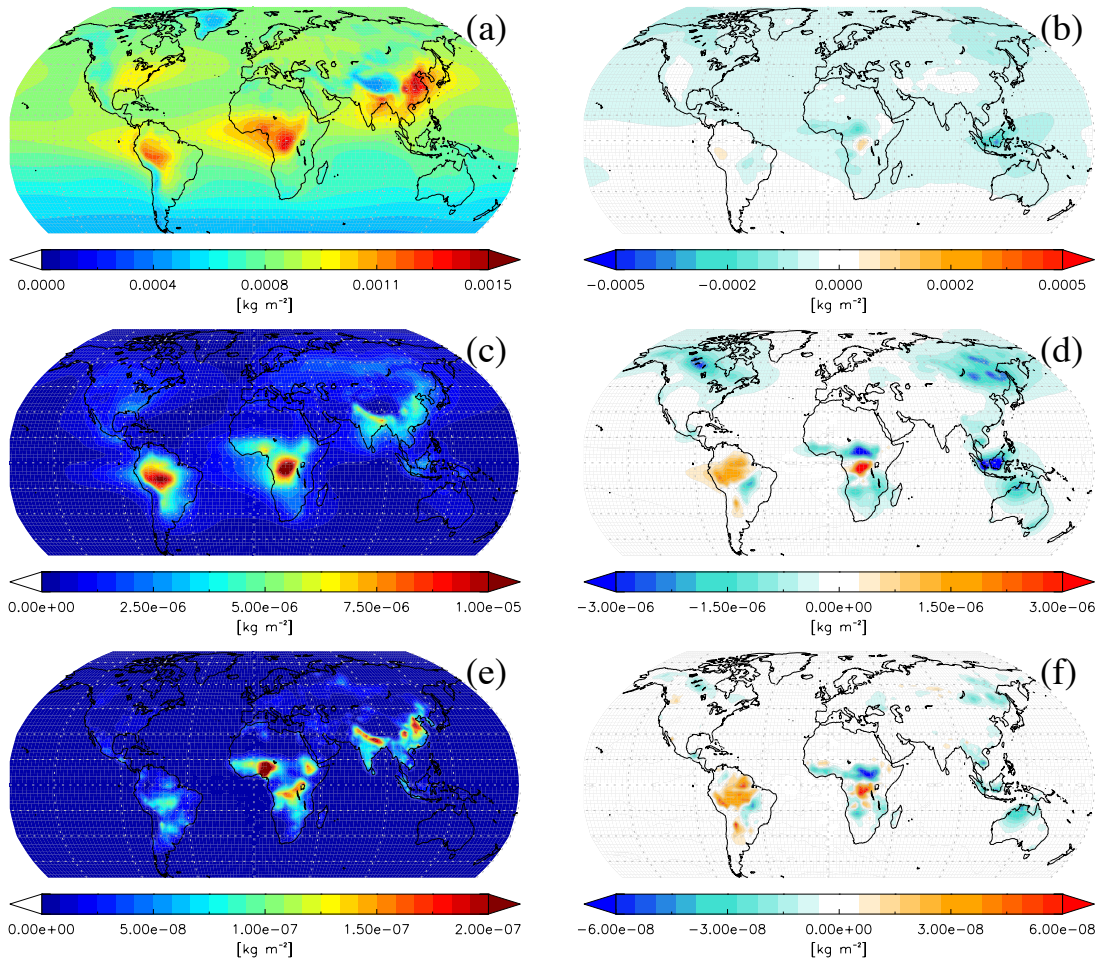
1289

1290 Figure 7: Annual mean model (left) and MODIS (right) active fires. Modeled annual
 1291 mean is based on an ensemble of 10 simulations. Simulated fires sampled at the daytime
 1292 Terra overpass time, 10:30am local time (a) and daytime Aqua overpass time, 1:30pm
 1293 local time (c). MODIS active fires are based on MODIS Terra (b) and MODIS Aqua (d)
 1294 from 2003-2016.



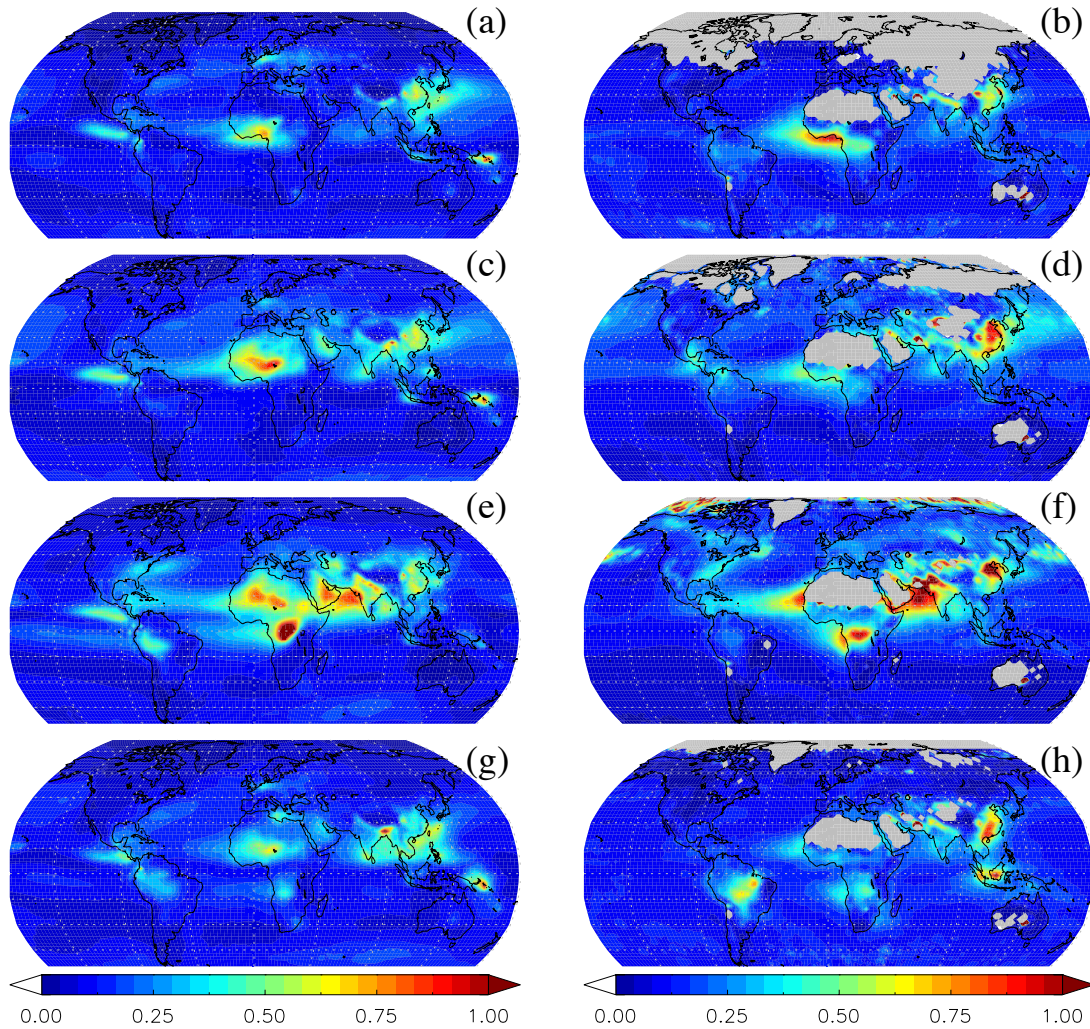
1295

1296 Figure 8: Annual mean model (left) and satellite based (right) active fires (a, b), burned
 1297 area (c, d), and CO emissions (e, f). Modeled annual mean is based on an ensemble of 10
 1298 simulations. Satellite detected active fires are based on MODIS Aqua retrievals of 2003-
 1299 2016, burned area is based on GFED4s inventory of 2003-2016, and CO emissions are
 1300 based on climatological GFED4s emissions of 2000-2010.



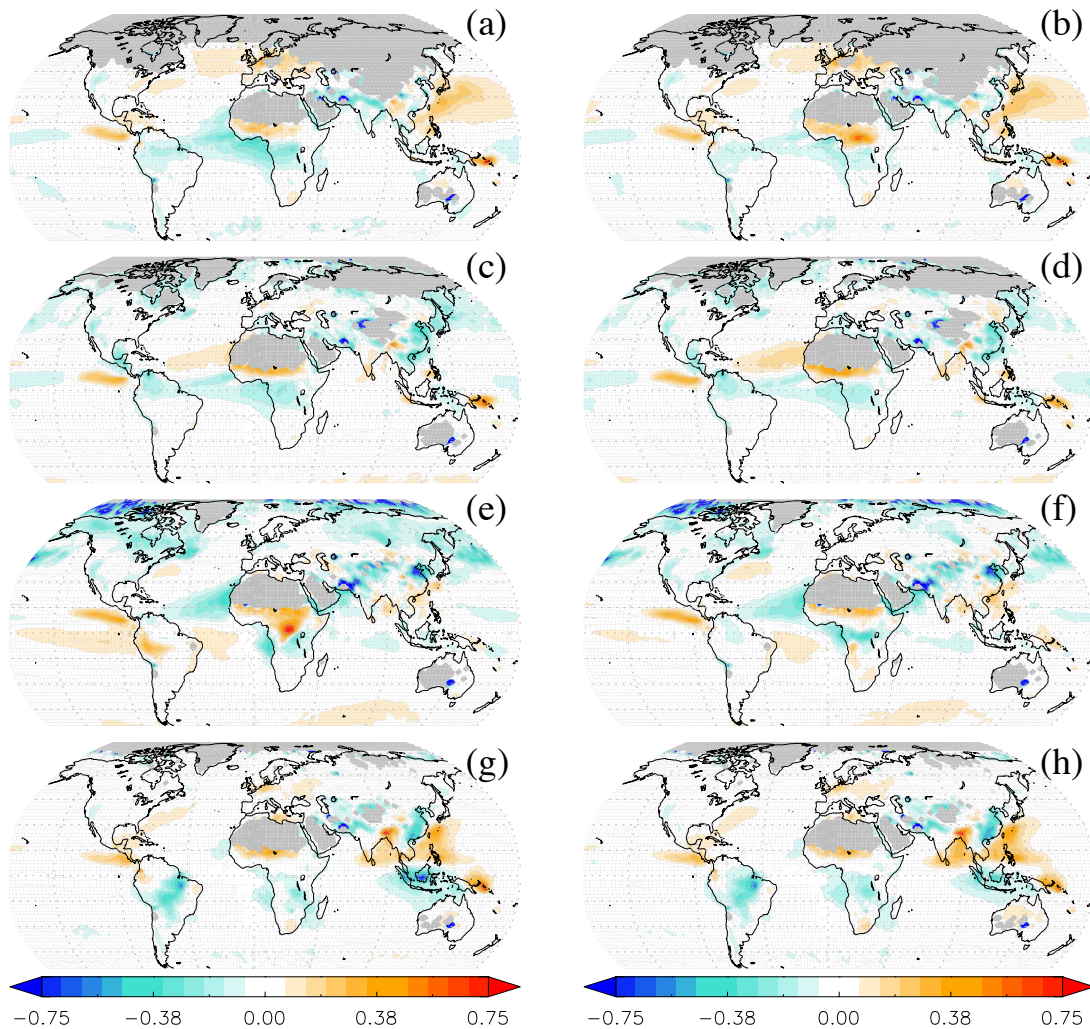
1301

1302 Figure 9: Modeled annual mean column density using pyrE fire emissions (left), and the
 1303 difference in column densities with a simulation using offline GFED4s emissions (pyrE -
 1304 GFED4s; right). CO (a, b), OA (c, d), and BC (e, f). Data based on an ensemble of 10
 1305 simulations.



1306

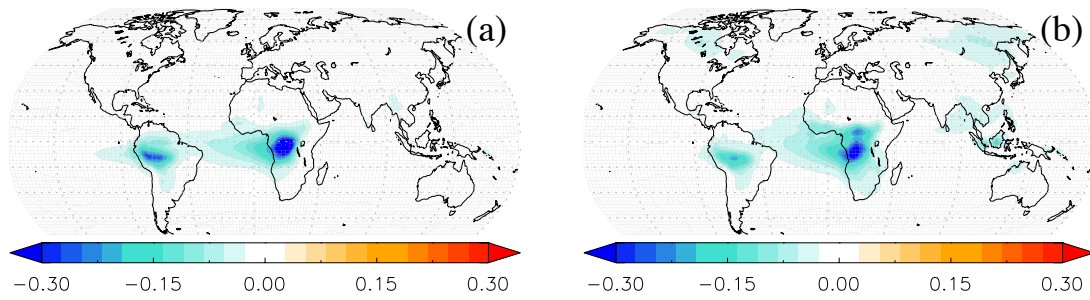
1307 Figure 10: Monthly modeled clear-sky aerosol optical depth (AOD) simulated using pyre
 1308 fire emissions (left), and detected by Aqua-MODIS (right). January (a, b), April (c, d),
 1309 July (e, f), and October (g, h). Monthly mean simulated AOD is based on an ensemble of
 1310 10 simulations, and climatologically monthly MODIS AOD is based on 2003-2007 data.
 1311 Missing MODIS data is shaded in light gray.



1312

1313 Figure 11: The difference in monthly modeled clear-sky aerosol optical depth (AOD) and
 1314 MODIS Aqua (model – satellite). Model simulations using pyrE fire emissions (left) and
 1315 model simulations using offline GFED4s emissions (right). January (a, b), April (c, d),
 1316 July (e, f), and October (g, h). The difference is based on an ensemble of 10 simulations
 1317 and 2003-2007 MODIS climatological monthly data. Missing MODIS data is shaded in
 1318 light gray.

1319



1320

1321 Figure 12: The difference in annual modeled clear-sky aerosol optical depth (AOD)
1322 between a simulation with no fire emissions to a simulation using pyrE fire emissions (a),
1323 and a simulation with offline GFED4s emissions (b). The difference (model with no fire
1324 emissions – model with fire emissions) is based on an ensemble of 10 simulations.

1325

1326

1327

1328

1329

1330

1331

1332

1333

1334

1335

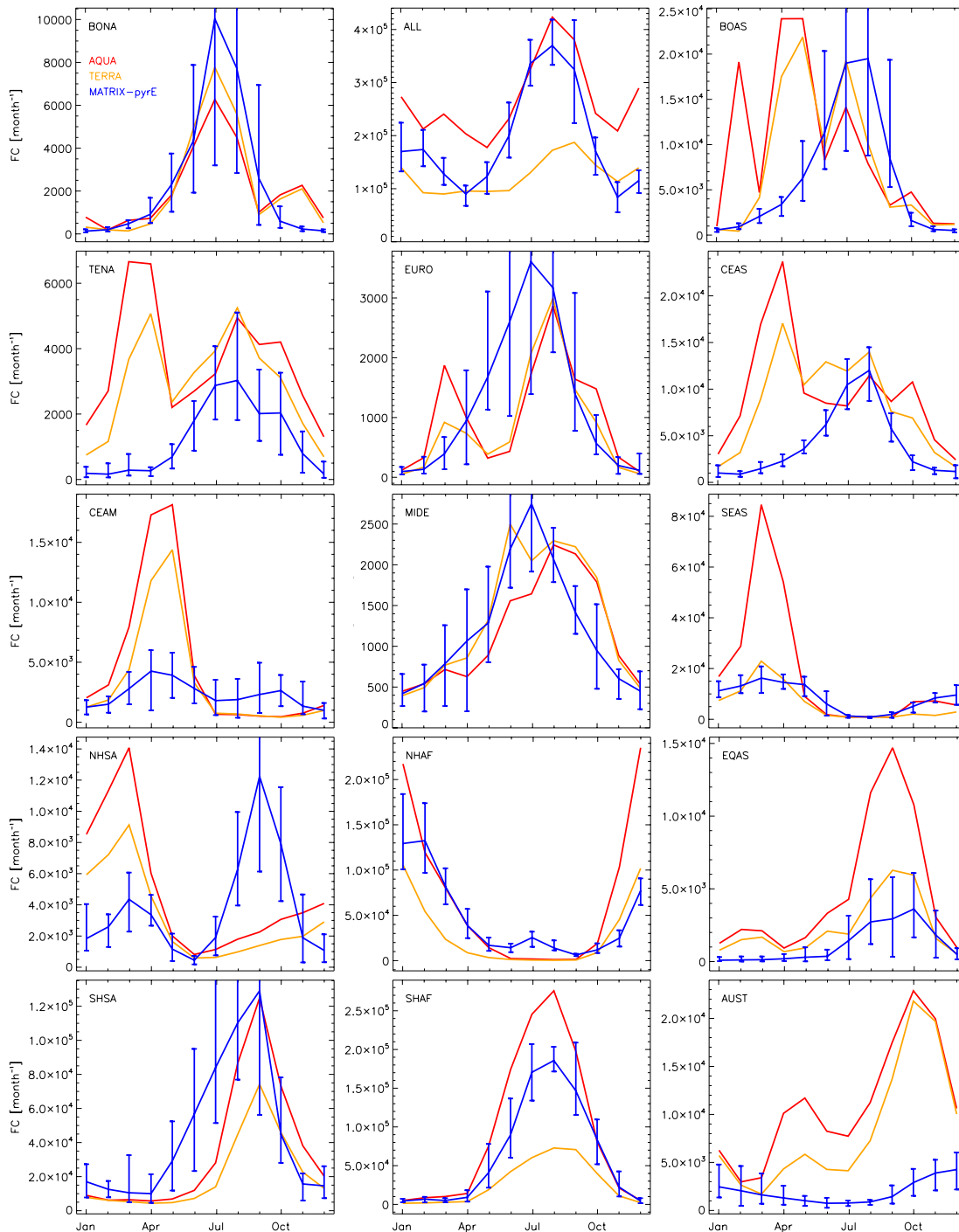
1336

1337

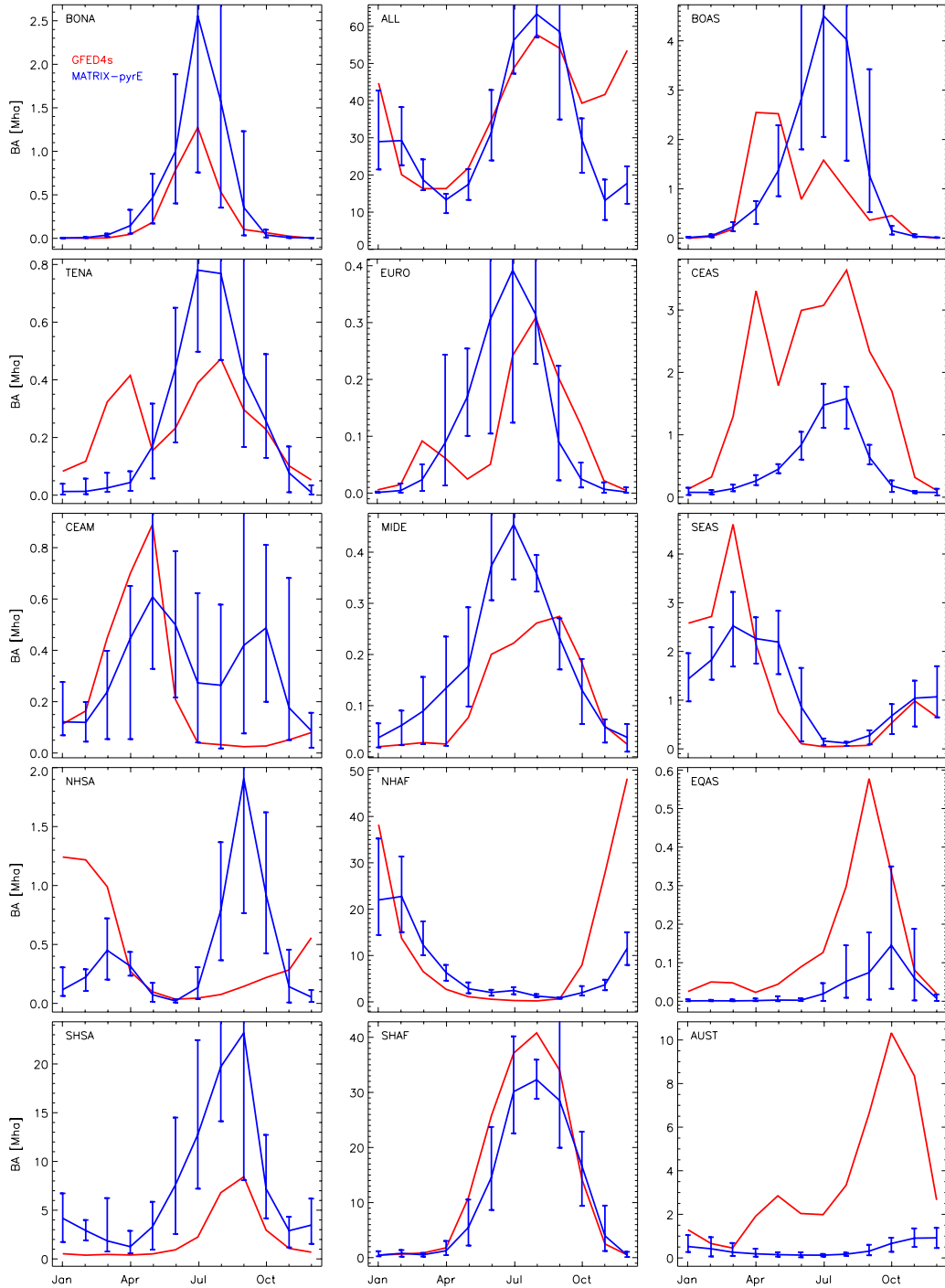
1338

1339

1340

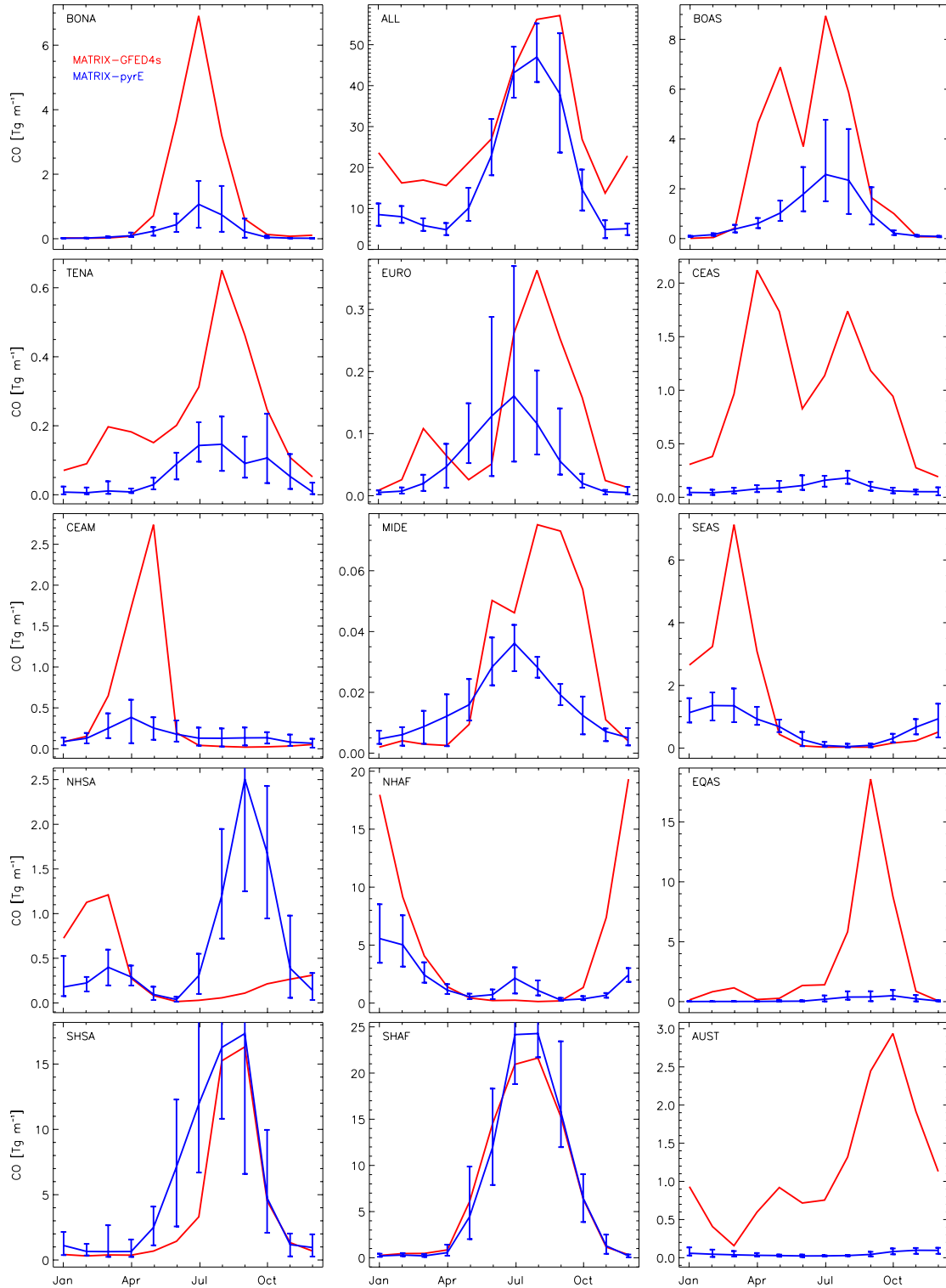


1342
 1343 Figure A1: Seasonality of total active fires (FC) detected by MODIS Aqua (red) and
 1344 Terra (orange) and simulated (blue) in all GFED regions (Fig. 1). Error bars represent the
 1345 10-year range in the simulations. Note the different scale in each panel.



1346

1347 Figure A2: Seasonality of total burned area; simulated (blue) and reported by GFED4s
 1348 (red) in GFED regions. Error bars represent the 10-year range in the simulations. Note the
 1349 different scale in each panel.

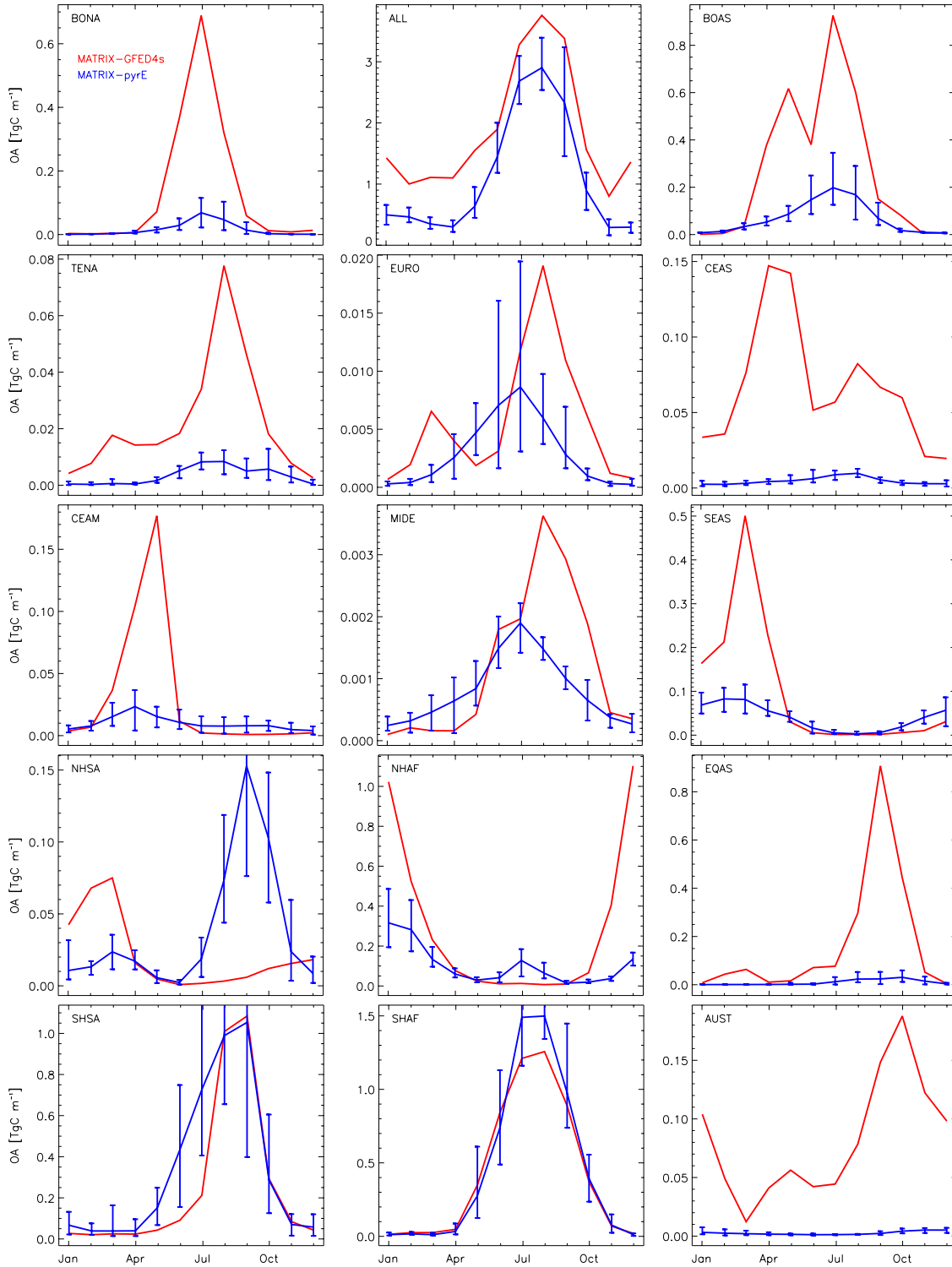


1350

1351 Figure A3: Seasonality of total fire CO emissions; simulated (blue) and reported by

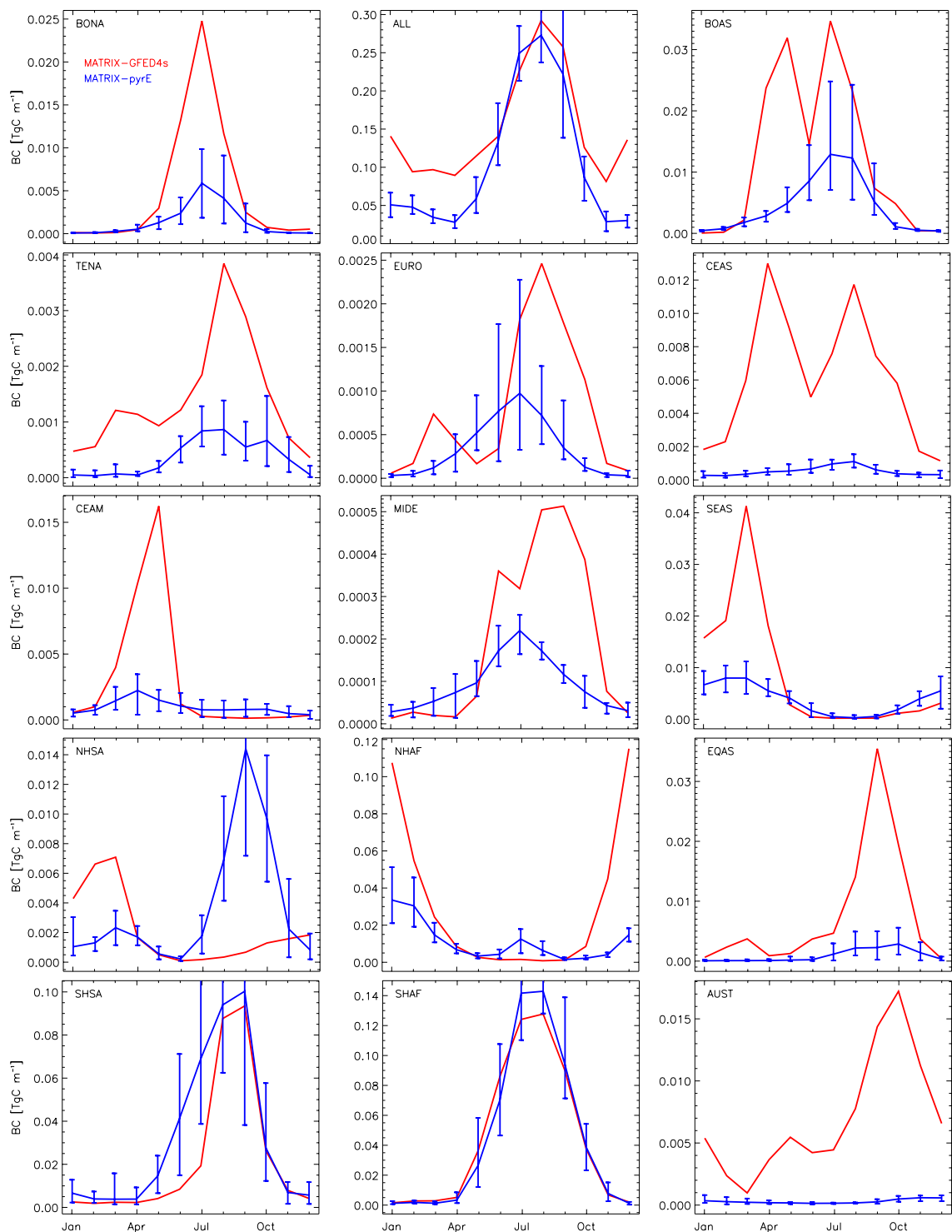
1352 GFED4s (red) in GFED regions. Error bars represent the 10-year range in the simulations.

1353 Note the different scale in each panel.



1354

1355 Figure A4: Seasonality of total fire organic aerosol (OA) emissions; simulated (blue) and
 1356 reported by GFED4s (red) in all GFED regions. Error bars represent the 10-year range in
 1357 the simulations. Note the different scale in each panel.



1358

1359 Figure A5: Seasonality of total fire BC emissions; simulated (blue) and reported by
 1360 GFED4s (red) in all GFED regions. Error bars represent the 10-year range in the
 1361 simulations. Note the different scale in each panel.